Axisymmetric cavities in hypersonic flow

Soumya R. Nanda [*]
Department of Aerospace Engineering, Indian Institute of Technology Kanpur, Kanpur 208016, Uttar Pradesh, India

Talluri Vamsi Krishna [†] and Jacob Cohen [‡]
Faculty of Aerospace Engineering, Technion-Israel Institute of Technology, Haifa 3200003, Israel

S. K. Karthick [§]
Department of Mechanical and Aerospace Engineering, Indian Institute of Technology Hyderabad, Kandi 502285, Telangana, India

(Received 19 February 2026; accepted 16 June 2026; published 14 July 2026)

A detailed experimental campaign is conducted to assess the shear layer characteristics of an axisymmetric open cavity configuration exposed to a Mach 6 freestream flow. Experiments are carried out in a Ludwieg tunnel across varying Reynolds number cases ($23\,000 \leqslant \mathrm{Re}_D \leqslant 74\,000$) based on the cavity depth (D). The influence of associated geometrical parameters in the form of length-to-depth ratio ($[L/D] = [2, 4, 6]$) and nondimensional excess height of the rear face with respect to the front face ($[\Delta h/D] = [-0.5, -0.25, 0, 0.25, 0.5]$) is assessed. Thereby, a detailed interpretation of the shear layer evolution is made based on qualitative flow structures captured using schlieren imaging and planar laser Rayleigh scattering (PLRS), along with quantitative measures obtained through unsteady pressure probes. Regardless of the $[L/D]$, the state of the shear layer is observed to be laminar at lower Re_Ds, and when increased, reveals the presence of Kelvin-Helmholtz (K-H) vortices. Nevertheless, for the longest aspect-ratio case ($[L/D] = 6.0$), the shear layer transitions to turbulence in the extreme Re_D cases owing to the availability of a longer length scale for K-H propagation. The spectral content obtained from the pressure response and the light intensity from the PLRS snapshots reveals an increase in the dominant frequency from the first Rossiter mode to higher-order modes for $[L/D] = 6.0$. Apart from $[L/D] = 6$, $[\Delta h/D] = 0$, the dominant frequency for all the cases considered herein matches the prediction of Rossiter modes and is found to be invariant of Reynolds number. While varying the $[\Delta h/D]$, shifting of modes occurs as obtained using proper orthogonal decomposition analysis of PLRS snapshots. For the negative $[\Delta h/D]$, the K-H mode is dominant (fifth and sixth Rossiter modes), whereas for the positive, the strong flapping mode (first Rossiter mode) prevails owing to significant pressure build-up inside the cavity recirculation region. For $[\Delta h/D] = 0$, both modes may coexist depending on Re_D. The azimuthal uniformity of the flow is also probed, indicating

[*]Contact author: soumyananda224@gmail.com
[†]Contact author: sri.vamsi1432@gmail.com
[‡]Contact author: aerycyc@technion.ac.il
[§]Contact author: skkarthick@mae.iith.ac.in

the dominance of the axisymmetric mode in the flapping scenario and much less correlated behavior in the case of K-H vortices in the shear layer.

DOI: 10.1103/dd1b-vlp7

I. INTRODUCTION

Cavities in high-speed flows have crucial aspects owing to the complex interaction of associated shock waves, separated shear layers, and the recirculation region [1]. Cavities find applications in various areas, including landing gear housings [2], weapon bays [3,4], scramjet components [5], flow control [6], and flame stabilization [7,8], among others. The cavity dynamics, specifically shock-shear layer interaction and recirculation bubble characteristics, vary significantly due to compressibility effects as the Mach number is changed, resulting in an unsteady flowfield in most cases, accompanied by spanwise coherent vortices [9,10]. The current investigation focuses on hypersonic flow past an axisymmetric cavity, which often finds application in both small- and large-scale contexts, such as sensor housing provisions[11] and trapped combustor [12]. Nevertheless, the applicability point of view differs in both cases. Small-scale cavities are used as a thermal shielding mechanism to isolate the sensors from the elevated heating zone, providing a laminar separated shear layer that results in reduced heat transfer [13]. Large-scale cavities, however, are typically used to aid rapid flow mixing. Moreover, upon reattachment of the separated flowfield, a hotspot forms [14] in the cavity's trailing edge. The transition from a laminar to a turbulent state in the incoming shear layer results in a further increment in the trailing edge heat load [15]. Therefore, it is essential to comprehend the state of the shear layer, its characteristics, and potential interaction mechanisms with the cavity's trailing edge, which may trigger unsteadiness.

The overall cavity flow is typically governed by the feedback loop of shear layer impingement on the aft wall, along with the generation and upstream propagation of acoustic waves, which then perturb the shear layer, thereby completing the feedback cycle [16]. The perturbations introduce vortical structures in the shear layer through K-H instability, which, when in a proper phase with the acoustic waves, results in a strong resonance leading to self-sustained oscillations, referred to as Rossiter modes [17–19]. The incoming flow properties and the geometrical parameters concerning the cavity are among the key attributes that drive the overall flow oscillation. Rossiter [17], followed by Heller *et al.* [20], proposed a semiempirical relation to predict the associated resonance frequency, which is presented in terms of the Strouhal number (St_D) as

$$\mathrm{St}_D = \left[\frac{fD}{u}\right] = \frac{(n-\alpha)(D/L)}{M(1+[(\gamma-1)/2]M^2)^{-1/2} + 1/\kappa}, \tag{1}$$

where M represents the Mach number of the flow upstream of the cavity, and the integer number $n = [1, 2, 3, 4, \ldots]$ indicates the mode number. The empirical constants $\alpha = 0.25$ and $\kappa = 0.57$ [10] correspond to the phase lag of the feedback loop, and the velocity ratio of the K-H convection to the freestream, respectively. It is to be noted that the empirical constant, $\kappa = 0.57$ was justified by Murray and Elliott [10] based on measurements of the convective velocity across a range of supersonic Mach numbers up to 3.5; therefore, in the present experiments the same value for κ is adopted. In general, the Rossiter mode numbers represent a spectrum of coupled acoustic-hydrodynamic oscillations, where the mode number determines the number of vortices along the shear layer between the leading and trailing edge (number of wavelengths). This suggests that for a given initial momentum thickness, the longer the shear layer spanning the cavity, the associated Rossiter mode number will increase [19]. The first Rossiter mode ($n = 1$) frequently described as the bulk motion of the separated shear layer which flaps to facilitate mass exchange between the cavity and the freestream [21]. As the mode number increases ($n = 2, 3$), both global shear layer oscillation (flapping) and convective instability (K-H vortices) mechanisms coexist, thereby exhibiting larger-scale coherent vortical structures convecting along the shear layer [22].

In the case of higher Rossiter modes ($n \geqslant 4$), the shear layer favors shorter streamwise wavelength K-H vortices (the associated high-frequency). At higher Mach number, the coherence of the K-H structures is reduced [10]. Amplification or stabilization of the Rossiter modes is typically reported for varying geometric situations (cavities with negative and positive asymmetry [23]) and incoming flow compressibility [24]. In contrast, cavity flows in relatively higher supersonic flow regimes are observed to be driven by the contribution of additional waves in excess of the impingement of the trailing-edge vortices [25]. The additional wave structures arise from the differences in the relative speed of the convecting large-scale structures with respect to the freestream flow and the internal cavity flow [26]. An increase in the Mach number also led to the dominance of three-dimensional (3D) modes over two-dimensional (2D) modes [27–29].

Two-dimensional cavities are relevant to real-world applications and can also serve as a canonical model to capture complex fields. Several researchers have investigated such cavities across various Mach numbers, Reynolds numbers, and cavity geometries. Recently, modal and resolvent analysis have helped establish the K-H growth rates [30] and cross-frequency interactions involving energy transfer from the fundamental Rossiter mode to harmonic modes [31], thereby identifying the flow behavior as convectively amplified or highly oscillatory. The stability analysis [19,32] is reported to demonstrate the significance of 2D Rossiter modes, along with 3D eigenmodes, including centrifugal instabilities and spanwise structures, in longer cavities. The evolution of tornado-like structures [33] and suppression of turbulence intensity with increase in Mach number [1] also happens to be altering the dominant spectral content through disruption of coherence in Rossiter modes. Most of the available literature emphasizes the interplay between compressibility effects, modal instabilities, and three-dimensional structures in the evolution of flow in two-dimensional cavities [34].

Although 2D cavity configurations have been extensively investigated across various flow regimes, their axisymmetric counterparts appear to be less explored. In the case of 2D planar cavities, where the spanwise coherence of vortical structures plays a crucial role [35], acoustic wave propagation is primarily unidirectional due to the coupling between vortex shedding and pressure resonance. Nevertheless, in axisymmetric cavities, information can propagate in the azimuthal direction, potentially altering the cavity dynamics as a whole. Recently, due to the growing interest in developing hypersonic propulsion systems [36] and redistributing thermal loads on reentry vehicles [37], the axisymmetric cavity has emerged as a more practical approach. Jackson *et al.* [38] investigated annular cavity configurations at varying aspect ratios for an incoming Mach number of 8.9 and reported a laminar nature of the shear layer for the shorter cavities, and transitional for $[L/D] = 8$. For longer cavities, three-dimensional unsteadiness is observed, likely due to the formation of a Taylor-Gortler instability. Similar research was undertaken by Creighton and Hillier [39], where different aspect-ratio cavities were mounted on a cone and exposed to an incoming flow with a Mach number of 5.5. The observed shear layer motion is classified as steady, mildly unsteady, and highly unsteady for different $[L/D]$ cases in conjunction with variation in the ratio between the upstream cavity length (L_F) and the length of the cavity (L_C). Based on that, the following criterion was deduced to label the flow unsteadiness,

$$\frac{L_C}{L_F} \approx 2\left[\frac{\tan(\beta - \theta)}{\tan(\mu) - \tan(\beta - \theta)}\right], \tag{2}$$

where $\theta,\ \beta,\ \mu$ are the cone angle, leading edge shock wave angle, and Mach angle, respectively. Additionally, it was noted that for the highly oscillatory shear layer case, the axisymmetry of the flow is preserved. In contrast, for the mild unsteady cases, a poor correlation is observed between the symmetric pressure sensors. The nature of the unsteady shear layer, in particular, has a potential that can manifest complex wave propagation within the cavity and result in the shifting of Rossiter modes. Interestingly, the Rossiter mode, which enables the identification of resonant frequencies in cavities, is also independent of the incoming flow Reynolds number [40].

Most of the existing cone-cavity studies do not account for the effect of the Reynolds number on the shear layer characteristics and acoustic feedback mechanism. In this context, the present study aims to systematically investigate the characteristics of the shear layer and its associated unsteadiness. An axisymmetric cavity mounted on a cone with a semiapex angle of 24° and a provision for varying the length-to-depth ratio as $[L/D] = [2, 4, 6]$ is considered for conducting a detailed experimental campaign. The influence of the reattachment surface is particularly explored by varying the normalized excess height of the rear cavity face as $[\Delta h/D] = [-0.25, 0, 0.5]$. These geometric variations of the cavity, along with a wide range of Reynolds number cases ($23\,000 \leqslant \mathrm{Re}_D \leqslant 74\,000$), are investigated for a freestream design Mach number of $M_\infty = 6$. Qualitative methods, such as schlieren and Rayleigh scattering-based imaging, are used in conjunction with quantitative measurements from unsteady pressure transducers to characterize the overall flowfield. This enables us to better understand the self-sustained oscillation pattern, along with the possible mechanism of driving the unsteadiness in axisymmetric cavity flows.

II. EXPERIMENTAL METHODOLOGY

A. Ludwieg tunnel facility description

The Ludwieg tunnel facility is utilized to understand the unsteadiness associated with hypersonic axisymmetric cavity flow, owing to its relatively longer test time compared to other impulse facilities. Hypersonic Ludwieg Tunnel (HLT) [41] located at Technion Israel Institute of Technology, Israel [see Fig. 1(a)] is used for the present set of experiments where the driver tube pressure is varied between 3 and 10 bar to generate a wide range of Reynolds numbers. The "U" tube configured driver tube, with an overall length of 3 m, is connected to a fast-acting valve that separates the tube from the convergent-divergent (C-D) nozzle, designed for a Mach number of $M_\infty = 6.0$, and the free-jet enclosed-test section. The exit diameter of the nozzle is $D_e = 76.2$ mm, out of which the flow is uniform within 60% of the jet core for about $[x/D_e] \approx 1$ [41] from the nozzle exit. Additional information on the procedure to estimate the extent of the uniform flow and the associated fluctuation levels in the test section, the reader is referred to the supplementary section of Karthick *et al.* [41]. Dry air is used as the test gas for all test cases, except for specific experiments where the test flow is seeded with CO_2 to facilitate necessary visualizations. Also, more details about the experimental facility, and detailed instrumentation can be found in the authors' previous work [41]. The steady test time for which the flow is expected to be constant can be inferred from the stagnation pressure (p_{01}) signal obtained at a location upstream of the C-D nozzle, as shown in Fig. 2-I. Observed $[p/p_{01}]$ is constant for ≈13 ms, during which the overall fluctuation level is also limited to $\sigma \approx 0.66\%$. Repeatability of the acquired responses across the runs can also be confirmed from Fig. 2-I.

Local pressure measurements are also performed on an axisymmetric cone without and with a cavity (in terms of a slot) at locations 2.6D and 10.6D along the cone surface from the leading edge, where D corresponds to the cavity depth of 4 mm (see Fig. 3). The selected locations are intentional, as they help identify the state of the upstream and downstream boundary layer to the cavity. The fluctuation level is limited to 2% for both the locations on the plain cone [see Figs. 2-II(a) and 2-II(b)], and also the similarity in both the signals is evident. Such low disturbance levels are generally associated with laminar or weakly disturbed hypersonic boundary layers, as reported in previous investigations on hypersonic transitional flows [42]. With the introduction of the cavity in the cone, the upstream pressure [Fig. 2-II(c)] still pertains to the root-mean-square (rms) level of 2%, whereas the downstream location [Fig. 2-II(d)] indicates a significant fluctuation intensity of about 5.8%.

B. Model details

Axisymmetric cavity configurations with desired geometric parameters are carved out in the form of an annular region, having a depth of $D = 4$ mm, from a conical model with an apex angle of $2\theta = 48°$ and a base diameter of 40 mm (see Fig. 3). The slant length of the cavity-mounted cone is ≈49 mm, and the cavity is placed in such a way that the cavity center is always at a fixed distance of

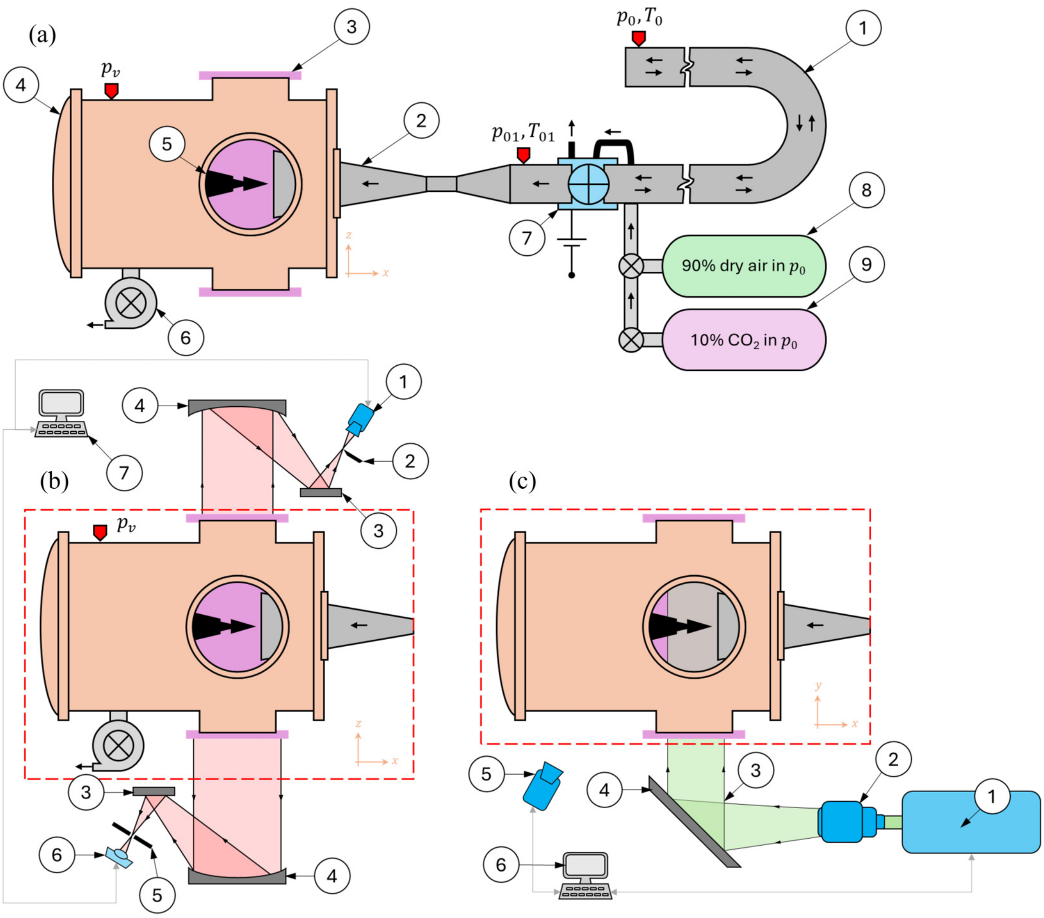

FIG. 1. (a) A typical schematic showing the short-duration hypersonic Ludwieg tunnel at Technion. Key components: (1) driver tube, (2) converging-diverging (C-D) nozzle, (3) view/optical ports, (4) dump/vacuum tank, (5) model mounting station, (6) vacuum pump, (7) fast-acting valve, (8) dry-air cylinder, and (9) CO_2 cylinder; (b) schematic showing the high-speed schlieren imaging setup. Key components: (1) high-speed camera, (2) knife edge, (3) plane mirror, (4) parabolic mirror, (5) slit, (6) light source, and (7) computer; (c) schematic showing the high-speed planar laser Rayleigh scattering setup. Key components: (1) continuous wave laser (532 nm), (2) sheet optics + collimator, (3) thin laser sheet, (4) plane mirror, (5) high-speed camera, and (6) computer.

6.6 D from the leading edge, as depicted in Fig. 3. The length-to-depth aspect ratios of the cavity are $[L/D] = [2, 4, 6]$, which correspond to different values of $[L/L_F] = [0.36, 0.87, 1.67]$. To assess the effect of the reattachment surface on the overall flow evolution, the height of the trailing edge is decreased as well as increased relative to the leading edge cavity depth ($[\Delta h/D]$) for $[L/D] = 6$, which results in $[\Delta h/D] = [-0.5, -0.25, 0, 0.25, 0.5]$. However, in the present study, we mostly concentrate on the cases of $[\Delta h/D] = [-0.25, 0, 0.5]$, are reported. Experiments are carried out for a set of Reynolds numbers based on the cavity depth $\mathrm{Re}_D = [23, 30, 38, 45.2, 51.3, 59, 66.3, 74] \times 10^3$ by varying the pressure in the driver tube. To better characterize the incoming boundary layer condition at the cavity leading edge, the Reynolds number based on the streamwise distance from the cone tip to the cavity leading edge (Re_x) is calculated. For the maximum driver tube stagnation pressure condition ($p_0 = 10$ bar), the estimated Re_x values for $L/D = [2, 4, 6]$ corresponds to $[4.1 \times 10^5, 3.41 \times 10^5, 2.66 \times 10^5]$, respectively. The values of Re_x further support the inference

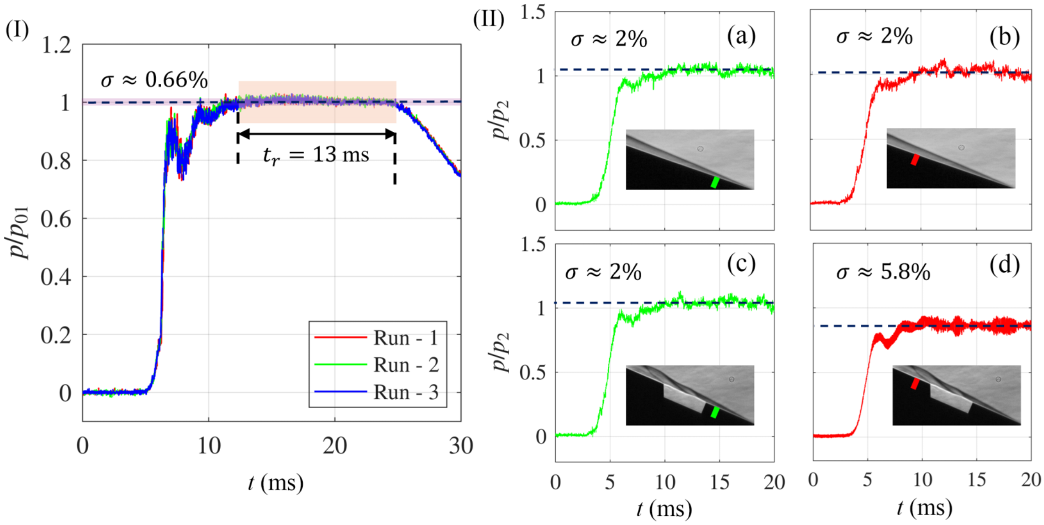

FIG. 2. (I) Typical pressure plot depicting the repeatability of the signal obtained from a location just upstream of the C-D nozzle. The fluctuation intensity (σ) across the runs for p/p_{01} is found to be $\approx$0.66%. (II) The local pressure depicting the fluctuation levels at the indicated locations marked in the snippet for the plain cone (a), (b) and the cavity-mounted cone (c), (d). p_2 corresponds to the static pressure post the conical leading edge shock, as can be referred from Table I. t_r refers to the run time for which the incoming pressure is found to be approximately constant.

that the incoming boundary layer upstream of the cavity is laminar. Moreover, the ratio between the momentum thickness (θ_0) at the cavity leading edge and the depth of the cavity (D) is an important parameter toward dictating the shear layer thickness along with the wavelengths of the K-H vortices and the associated Rossiter numbers. However, in the present experimental setup, it is not possible to reliably estimate the momentum thickness experimentally due to the extremely thin incoming boundary layer over the axisymmetric cone. Therefore, θ_0 is calculated using the freestream conditions and upstream distance to the cavity leading edge (L_F) in conjunction with

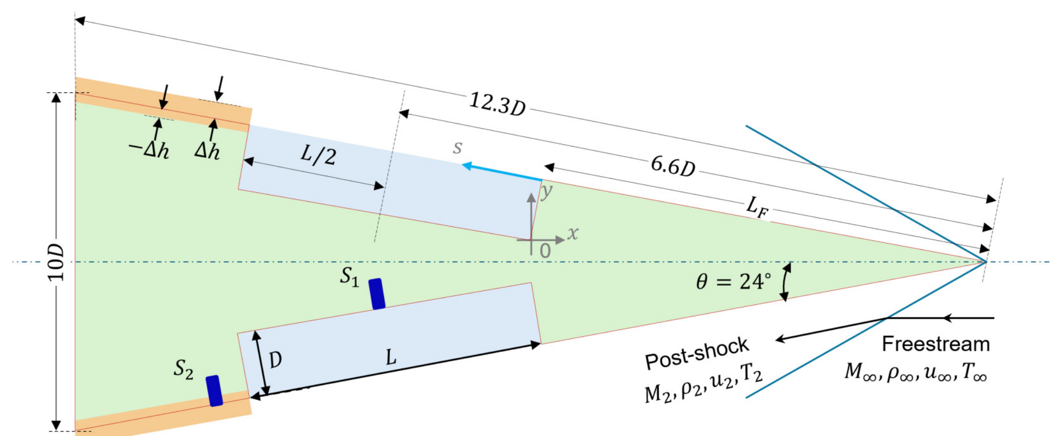

FIG. 3. Schematic of the cone-mounted cavity configuration, highlighting the key dimensions and cavity nomenclatures used in the present study. L_F will be different based on the $[L/D]$. S_1 and S_2 correspond to locations of the unsteady pressure probes.

TABLE I. Derived flow parameters in the freestream and cavity upstream for the extreme cases of driver tube and stagnation pressures (p_0 and p_{01}), using the isentropic relations.

Parameters	Freestream (∞)	Cavity upstream (2)
Static pressure (p, Pa)	152.64–514.92	1472–4785
Static temperature (T, K)	36.58	91.6
Static density (ρ, kg/m^3)	0.015–0.049	0.056–0.182
Kinematic viscosity ($\nu \times 10^{-5}$, m^2/s)	14.7–4.4	11.2–3.4
Velocity (u, m/s)	727.46	636.93
Shock angle (β for $\theta = 24^\circ$, deg)		28.3
Mach number (M, –)	6.0	3.32
Reynolds number (Re$_D \times 10^3$, –)	19–67	23–74

the Blasius solution for compressible flow assuming a 2D laminar boundary layer upstream to the cavity. The value of D/θ_0 is calculated to be within a bound of [44–80], [48–88], and [55–100], for $L/D = [2, 4, 6]$, respectively, across the cases of Re$_D$ considered herein. The ratio D/θ is of the order of 100, which justify the use of the 2D approximation. All experiments are conducted under room temperature conditions, limiting the total enthalpy to 0.3 MJ/kg. The flow conditions prevailing in the freestream flow, as well as the cavity upstream, are estimated using isentropic and conical shock relations, which are presented in Table I.

C. Measurement methodology

The present study involves both high-resolution and high-repetition-rate imaging to identify the overall flow evolution and quantify the associated unsteadiness. High-resolution schlieren imaging [see Fig. 1(b) for the set-up] is performed to capture the transverse density gradient ($\partial\rho/\partial y$) through a conventional "Z-type" setup [43] using an LED light source. A high-speed camera is used to capture the spatial field at a frame rate of 2.2 kHz corresponding to a resolution of 1280 × 800 pixels and an exposure time of 2 µs. Typical schlieren snippet for a plane cone flow and cavity-mounted cone is displayed in Figs. 4-I(a) and 4-I(c). For the semicone apex angle of $\theta = 24^\circ$, the leading edge shock angle is measured to be 28.4° for the flow over plain cone [Fig. 4-I(a)], which is a 0.2% deviation from the estimation using Taylor Maccoll relation. The high-resolution image of the axisymmetric cavity [Fig. 4-I(c)] shows undulations along the shear layer, which will be discussed in the subsequent sections. To better understand the unsteadiness, space-time (y-t) plots are constructed; however, they may not provide a clear picture [see Fig. 4-I(d)] when applied to high-resolution spatial images. The y-t plots [Figs. 4-I(b) and 4-I(d)] are generated by stacking the light intensity variation over a desired time interval along the profiles marked by the yellow dashed lines in the Figs. 4-I(a) and 4-I(c), which also corresponds to the location for the cavity center. The leading-edge shock emanating from the cone tip appears fairly steady [Fig. 4-I(b)], indicating minimal incoming freestream turbulence to the cavity.

From the visualization perspective, the axisymmetric cavity geometry seems different [see Fig. 4-II(b)] as compared to the sectional view [see Fig. 4-II(a)]. This is attributed to the rotation of the sectional view about the x-axis and the light source being placed sideways to the cone-cavity model, for which the integrated effect looks like the cavity trailing edge being a vertical one as seen in Fig. 4-II(b). Hence, the cavity trailing surface appears to be vertical as shown in Fig. 4-II(b) for all the images presented in the subsequent sections, both from schlieren and Rayleigh scattering.

In contrary to schlieren imaging which yield a line-of-sight-integrated flowfield, planar measurements in a streamwise plane at $z/D = 0$ are obtained using the planar laser Rayleigh scattering (PLRS) technique [44] [see Fig. 1(c) for the set-up]. CO_2 gas is mixed with air in a proportion of 1:9 by volume in the driver tube, which upon expansion to the freestream conditions forms icicles typically of the order of 0.5 µm owing to the very low static temperature mentioned in

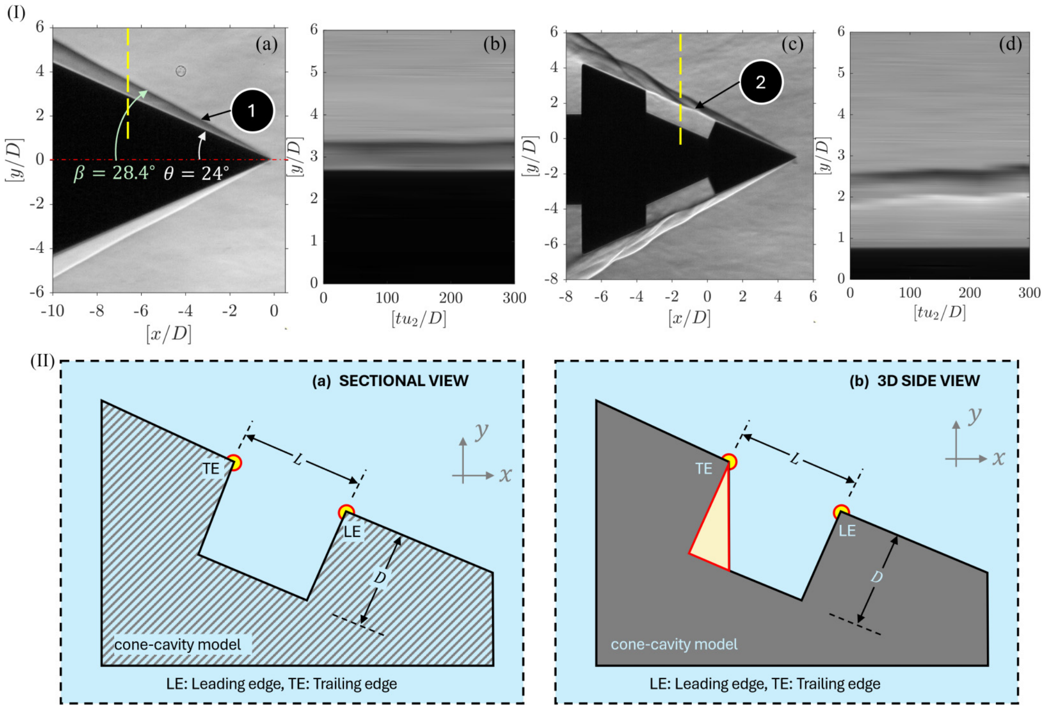

FIG. 4. I(a), I(c) High-resolution schlieren image obtained for plain cone flow, and cavity mounted cone, respectively, with vertical lines marking the profiles along which the space-time plots are construed; I(b), I(d) Typical space-time (y-t) diagrams, representation of the temporal fluctuations for the respective cases of plain cone and cone-cavity configuration. II(a) Sectional and II(b) 3D side view of the hypersonic cone-cavity to highlight the shadowing of the cavity near the trailing edge while rotating the model about the cone-axis. Cavity configuration corresponds to $[L/D] = 4,\ [\Delta h/D] = 0$, and incoming flow Re_D is 74 000. Flow features: (1) leading-edge shock, (2) separated shear layer.

Table I. PLRS relies on measuring the scattered light intensities from icicles when illuminated by a continuous laser of similar wavelength as the icicle size. It should be noted that it is not possible to capture the low-velocity region within the cavity using PLRS, as icicles tend to evaporate upon interacting with the relatively warmer fluid. High-repetition-rate PLRS images are captured at a resolution of 128×96, with a fixed acquisition rate of 100 kHz. Typical instantaneous PLRS for the attached flow over the plane cone, and the small-structure laded shear layer can be seen from Figs. 5-I(a) and 5-II(a), respectively. In a similar way as mentioned previously, y-t plots [Fig. 5(b)] are generated along with the corresponding y-f plot [Fig. 5(c)] through fast Fourier transform, depicting the dominant spectral content. No susceptible frequency is identified for the plane cone flow, as the broadened spectra seen in Fig. 5-I(c) is attributed to an anomaly of laser light reflection on the cone surface. However, a dominant frequency is identified in the case of an axisymmetric cavity [Fig. 5-II(c)], thereby indicating the capability to resolve the unsteadiness across the shear layer. More details about the schlieren and PLRS system can be found in Karthick *et al.* [41].

Local mean pressure variation and pertinent dominant spectral content across the cases are quantified using the unsteady pressure sensors (Kulite XCQ-080-100A) mounted on the cavity floor center (S_1 as depicted in Fig. 3) and on the cone surface downstream of the flow reattachment (S_2 which is at $10.5D$ from the leading edge). Pressure responses are recorded using NI data-acquisition cards at a sampling rate of 800 kHz. The location S_1 lies within the recirculation region beneath the separated shear layer, where the pressure field is relatively uniform. Measurement

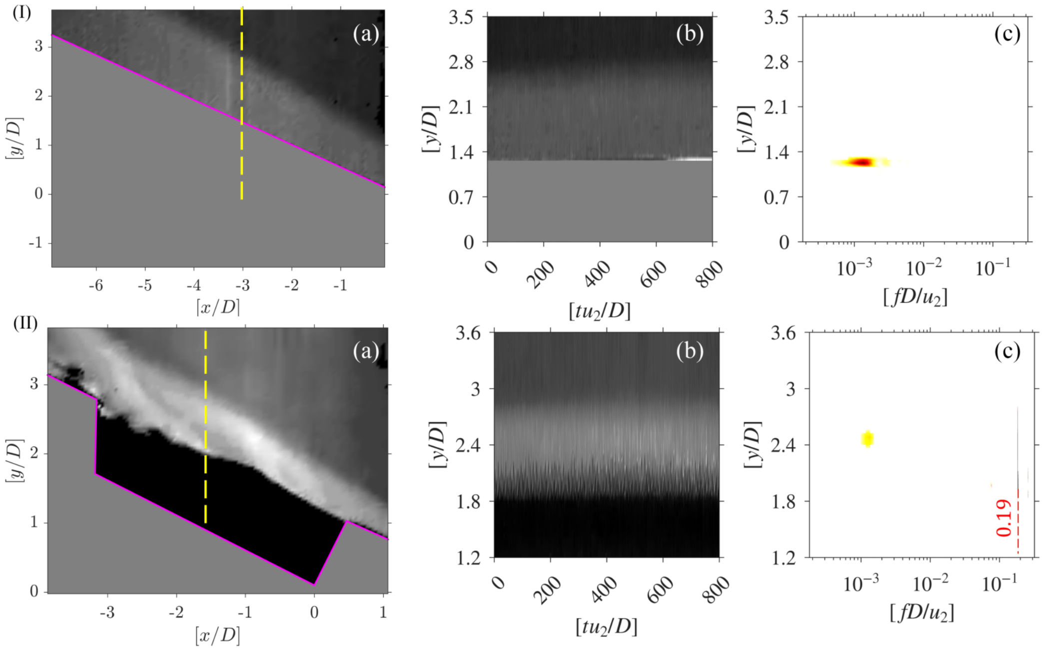

FIG. 5. Instantaneous (a) PLRS snapshot obtained during high-repetition rate imaging for (I) plain cone flow, and (II) cavity-mounted cone flow. (b), (c) represent respective space time (y-t), and space-frequency (y-f) plots. Cavity configuration corresponds to $[L/D] = 4$, $[\Delta h/D] = 0$, and incoming flow Re_D is 74 000.

at S_1 location enables robust estimation of the global unsteadiness associated with the cavity resonance mechanism, minimizing sensitivity to localized gradients near the leading or trailing edges. Moreover in open cavity flows, the pressure over a large portion of the cavity floor is generally reported to remain relatively uniform, with the most significant variation occurring near the trailing edge owing to reattachment induced pressure gradients. Therefore, the absolute magnitude of the measured pressure coefficient and fluctuation amplitude would vary depending on the exact sensor location; nevertheless, the variation across the central region of the cavity floor is expected to be comparatively smaller [38]. Similar sensor arrangement for measuring the open cavity response to geometric parameters is also adopted by Trudgian *et al.* [45]. The S_2 sensor is positioned in such a way that it is directly influenced by shear-layer deflection, vortex impingement, and reattachment shock dynamics which makes it particularly suitable for quantifying the downstream impact of cavity-induced unsteadiness. Similar downstream pressure measurement toward assessing the spectra and associated phase is carried out by Oka *et al.* [46].

D. Uncertainty quantification

Uncertainty estimation is a critical aspect to ascertain the variation in the parameters derived during the experimental campaign. The analysis accounts for contributions to uncertainty from systematic and random sources, including measurement accuracy, run-to-run variability, background noise, geometric tolerances, spatial resolution, and statistical dispersion associated with visually identified features [47]. The overall uncertainty in any parameter is calculated by aggregating individual contributing sources using a statistical-based root-sum-square methodology [48]. Primarily, the uncertainty in freestream conditions such as Mach number, pressure, and temperature is calculated based on Rayleigh-pitot and isentropic relations in conjunction with uncertainty in the driver tube pressure (p_{01}) and pitot pressure (p_{02}) measurement. Effectively, the uncertainty in freestream Reynolds number is calculated to be $\pm 3.4\%$. The high-repetition PLRS snapshots at the current settings yield a spatial resolution of 0.22 mm, resulting in an uncertainty of ±4.8% in the estimated onset location of convective structures in the shear layer. The frequency resolution of the PLRS-based estimate is 167 Hz, calculated from 600 frames during the test duration, whereas the resolution of the sensor-based estimate is 83 Hz. As a result, the variation in St_D is expected to be ±3.5% and ±2.5% for PLRS and sensor-based estimate, respectively. The uncertainty in nondimensional mean pressure variation, which is mainly contributed by the standard deviation across the runs, is about ±3.1%.

III. RESULTS AND DISCUSSION

Prior to experiments with the axisymmetric cavity, it is intended to gather information on the prevailing flow state on the cone surface. The high-resolution schlieren snapshot, along with an instantaneous PLRS image for hypersonic flow over the cone, is depicted in Figs. 4-I(a) and 5-I(a). It is clear from both figures that the flow remains attached to the entire cone surface and is free of any structures, thereby indicating predominantly laminar flow under the present operating conditions. Also, the y-f analysis [Fig. 5-I(c)] portrays no significant spectral content. From Figs. 2-II(a) and 2-II(b), it can also be ensured that the pressure values downstream of the leading edge shock have good agreement with those of the estimated conditions mentioned in Table I, and the fluctuation levels are within ±2%. Therefore, irrespective of the cavity location on the cone surface, laminar flow is expected at the cavity entrance. In the following section, the effects of geometric parameters and incoming flow conditions on the flow evolution are discussed, utilizing both qualitative and quantitative perspectives.

A. Effect of aspect ratios [L/D]

1. Qualitative interpretation

The schlieren images obtained using high spatial resolution imaging for several [L/D] and Re_D, having [$\Delta h/D$] = 0, are shown in Fig. 6. Instantaneous images are used to identify the gross flow features, allowing for the qualitative drawing of conclusions on the intensity of shock-related unsteadiness. Some of the key flow features evident from the schlieren snapshots are: the leading edge shock from the cone tip (marked as ① in Fig. 6), which makes the flow parallel to the cone surface, flow separation leading to the formation of a separated shear layer at the front cavity face (marked as ② in Fig. 6), and the reattachment shock emanating from the trailing edge (marked as ③ in Fig. 6). All [L/D] cases considered herein across the Re_D range portray a separated shear layer spanning the entire cavity length, indicating the typical characteristics of an open cavity configuration. Irrespective of the Re_D, a laminar separated shear layer with no evidence of vortex roll-up is perceived for [L/D] = 2 [Fig. 6(a)], which is also true for the lowest Re_D = 23 000, across the [L/D] cases (see Fig. 6-I). For [L/D] = [4, 6], further increase in Re_D results in the onset of convecting vortical structures [Fig. 6-II(b)] along the laminar shear layer, caused by Kelvin-Helmholtz (K-H) instability. These vortical structures is accompanied by weak Mach waves along the convecting direction of the supersonic stream (marked as ④), as well as acoustic waves in the recirculating subsonic zone. Also, the shock and separated shear layer motion intensify with an increase in Re_D, thereby significantly enhancing the reattachment shock's strength [Figs. 6-II(c) and 6-III(b)]. At the highest Re_D = 74 000 for [L/D] = 6 [Fig. 6-III(c)], acoustic waves originating from the trailing edge (marked as ⑤ in Fig. 6) and propagating into the cavity upstream are clearly visible (see the Supplemental Material [57] for the schlieren video acquired in high-repetition rate). This, in turn, amplifies the K-H vortices on the separated shear layer to grow spatially along the streamwise direction and eventually break down to a turbulent state. Disappearance of waviness in the separated shear layer marks the ending of the laminar shear layer [compare the white stripe in Figs. 6-III(b) and 6-III(c), also marked as ⑥ in Fig. 6]. The wave structures highlighted in Fig. 6-III(c) may appear slightly vertical, which is primarily a imaging artifact. Owing to axisymmetric geometry of the cavity, the disturbances propagating along the

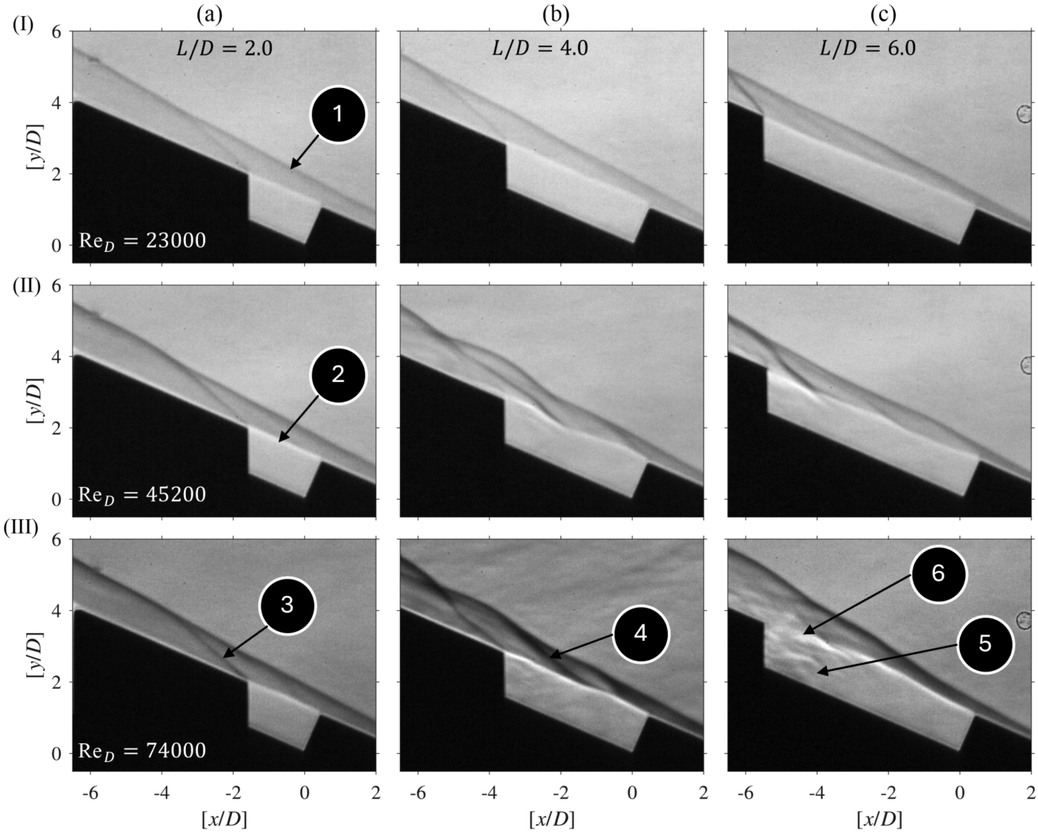

FIG. 6. Effect of length-to-depth ratio ($[L/D]$) at different Reynolds numbers (Re_D) on the overall flow features obtained through high-resolution schlieren imaging. Instantaneous schlieren images taken at an arbitrary time-step for different cases with no-excess trailing edge height case ($[\Delta h/D] = 0$) for: (a) $[L/D] = 2.0$, (b) $[L/D] = 4.0$, and (c) $[L/D] = 6.0$. Each row corresponds to a fixed value of Reynolds number where (I) $Re_D = 23\,000$, (II) $Re_D = 45200$, and (III) $Re_D = 74\,000$. Key flow features: (1) leading edge conical shock, (2) separated shear layer, (3) reattachment shock at the trailing edge, (4) shock wave from the undulating shear layer, (5) upstream propagation of acoustic waves, and (6) shear layer turbulent break-down. See the Supplemental Material [57] for the corresponding video files (top row is PLRS, bottom row is schlieren).

annular shear layer appear visually as slightly vertically oriented in the projected image, rather than purely streamwise oriented waves as typically observed in two-dimensional cavities. As only three cases of Re_D are shown in Fig. 6 for brevity, the exact transitional Re_D will be estimated during the analysis of high-speed PLRS snapshots. As mentioned earlier in Eq. (2), Creighton and Hillier [39] developed a criterion to determine the critical ratio of $[L/L_F]$ beyond which unsteadiness in the shear layer can be expected. Based on Eq. (2), for the current experimental scenario, the estimated critical $[L/L_F]$ is 0.568. In agreement with their prediction, the case of $[L/D] = 2$, for which the $[L/L_F] = 0.36$ indeed shows a steady flowfield, whereas for $[L/D] = [4, 6]$, the corresponding $[L/L_F] = [0.87, 1.67]$ are greater than the critical $[L/L_F]$ and both shear layers show unsteadiness.

Schlieren imaging is a line-of-sight integrated technique that does not capture some flow features, such as three-dimensional small-scale structures or the transition point in the separated shear layer in a given plane. Therefore, PLRS imaging is carried out for all the cases across Re_Ds but only shown for $[L/D] = 6$ in Fig. 7 at specific Re_D for brevity. It is noted that, for the lowest Re_D case, the snapshot appears hazy (due to poor light intensity) caused by the low-density field resulting

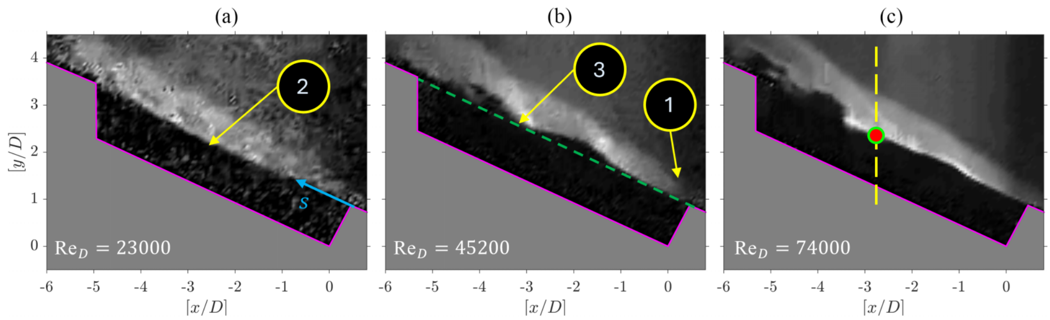

FIG. 7. Typical PLRS snapshot for different Re_Ds of (a) 23 000, (b) 45 200, and (b) 74 000 obtained for the case of $[L/D] = 6$. Key flow features: (1) conical shock from the leading edge, (2) laminar shear layer, (3) K-H vortices. See the Supplemental Material [57] for the corresponding video files.

from the low fill pressure conditions in the driver tube. A laminar shear layer (marked as ② in Fig. 7) spanning the cavity [Fig. 7(a)] is seen for most of the cases. However, for an increased Re_D for $[L/D] = 4$, small-scale K-H vortices are seen to be convected along the separated shear layer [see Fig. 5-II(a)]. For a fixed Re_D, the wavelength of the K-H vortices increases as $[L/D]$ increases [compare Figs. 5-II(a) and 7(c)], which is in line with earlier observations [29]. Moreover, the point of origin of these K-H vortices, where the shear layer is perturbed by the acoustic wave, seems to move further upstream along the shear layer as $[L/D]$ increases [compare Figs. 5-II(a) and 7(c)]. The shear layer perturbed location can be demarcated from the s-f plots as shown in Fig. 8, where the line profile considered is along the shear layer as marked in Fig. 7(b), where s is the line along the cavity shear line starting at the leading edge [see Figs. 7(a) and 7(b)]. With increases in Re_D from 23 000 to 74 000, the dominant frequency in each of the cases starts appearing from $[s/D]$ of 1.5 and 0.6, respectively. These estimates can be considered as the probable location for perturbation, as upstream of it, a laminar shear layer exists. With an increase in Re_D, the upstream movement of the perturbation location indicates the availability of a longer length (till the rear face of the cavity) for instability wave amplification and breakdown into turbulence. Nevertheless, with an increase in Re_D for $[L/D] = 6$ [see Fig. 7(c)], the wavelength of the K-H vortices is shortened, and their coherence seems to be fading out at some downstream point, thereby indicating the possibility of shear layer breakdown, which is apparent from the schlieren snapshot and upstream shear layer perturbation.

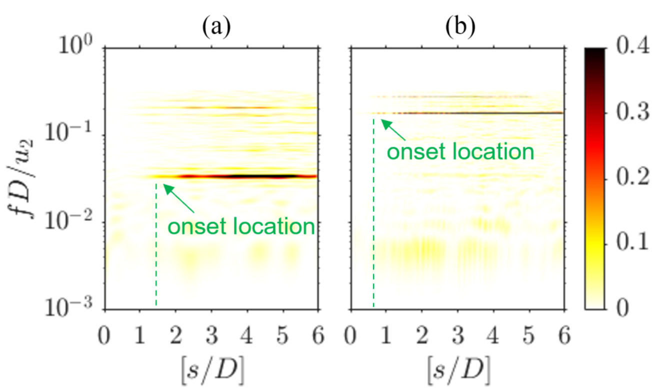

FIG. 8. s-f diagram generated for the case of $[L/D] = 6$ having (a) $Re_D = 23\,000$ and (b) $Re_D = 74\,000$ where the profile is generated along the shear layer. The respective line is marked in dashed green color in Fig. 7(b).

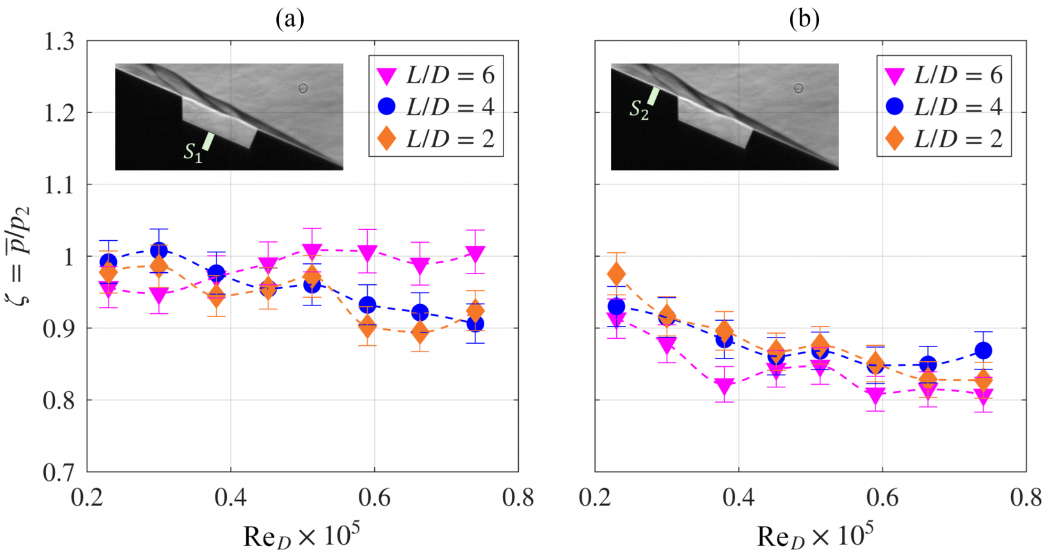

FIG. 9. Nondimensional mean pressure variation at the (a) cavity floor center, S_1, and (b) cavity downstream, S_2, location with change in $[L/D]$ and Re_D.

2. Quantitative estimation

The effect of cavity aspect ratio ($[L/D]$) with $[\Delta h/D] = 0$ is quantified for a range of Re_D in terms of the mean pressure variation ($\zeta = \overline{p}/p_2$, where p_2 corresponds to the static pressure downstream of the conical leading-edge shock as mentioned in Table I) at the cavity floor (S_1) and downstream cavity location (S_2) as shown in Fig. 9. For all cavity aspect ratios ($[L/D]$) considered herein, the mean pressure magnitude on the cavity floor varies in the range of $0.9 \leqslant \zeta \leqslant 1.0$ [see Fig. 9(a)], thereby signifying that the recirculation bubble entrapped by the separated shear layer and the cavity floor are almost in pressure equilibrium. Moreover, at lower Re_Ds, the pressure variation between $[L/D]$ cases is relatively lesser, and at the highest range of Re_Ds, the percentage of variation in ζ increases. For $[L/D] = 6$, at higher Re_Ds, the ζ is found to be almost 1, which is probably a result of better mixing and interaction with the freestream flow due to the turbulence breakdown of the shear layer as seen during the high-resolution schlieren imaging [Fig. 6-III(c)].

Similarly, at the downstream cavity location S_2, owing to the interaction of the vortices with the trailing edge followed by the reattachment shock oscillation, inability of the pressure recovery is evident for $[L/D] = [2, 4, 6]$ at most Re_Ds, thereby resulting in a lesser mean pressure downstream of the cavity [Fig. 9(b)]. Irrespective of the $[L/D]$, an overall decrement in magnitude for S_2 location is observed with increases in Re_D. For lower Re_D cases, weaker density gradient near the trailing edge [Figs. 6-I and 6-II(a)] indicates possibility of gradual flow turning, and more effective pressure recovery leading to similar magnitudes at the S_1 and S_2 locations across $[L/D]$s. With increment in Re_D, owing to the occurrence of the convecting K-H vortices [Figs. 6-II and 6-III(b)], reattachment happens over an extended streamwise region followed by distributed flow turning and expansion, leading to lesser ζ. Moreover, apart from $[L/D] = 6$, all the other cases experience less than $\pm 8\%$ variation between pressure level on the S_1 and S_2 location across the entire Re_D range considered herein. For $[L/D] = 6$, the S_2 location is found to have $\approx 20\%$ lesser mean pressure in comparison to the S_1 for higher Re_Ds. At higher Re_Ds, the shear layer transitions to turbulence, resulting in a weaker reattachment shock than in other cases, which can explain lower pressure at the S_2 location.

The dominant frequency is identified from pressure responses measured at location S_1 during the run-time through fast Fourier transform (FFT) analysis. In parallel, to support the analogy from the unsteady visualization, a point on the cavity shear layer at the cavity centerline is

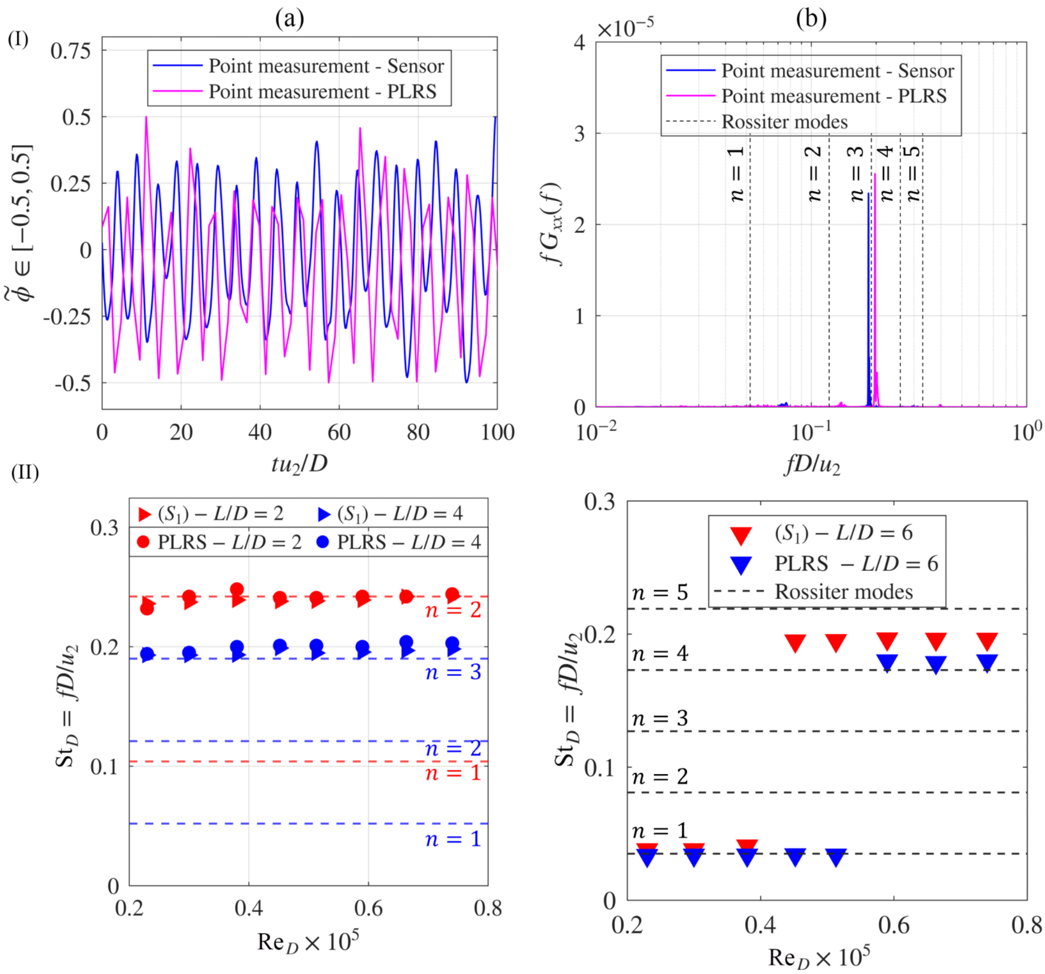

FIG. 10. I(a) Rescaled fluctuation levels ($\tilde{\phi}$) obtained during the run-time from PLRS imaging on the shear layer [see Fig. 7(c) for the location] and from the sensor S_1 placed on the cavity floor center for the case of $[L/D] = 4$ at $\mathrm{Re}_D = 74\,000$. I(b) The spectra obtained using FFT on the normalized fluctuations signal depicting the dominant St_D from both the techniques and their agreement with the predicted frequencies of the Rossiter modes. (II) Comparison of dominant St_D obtained from sensor (S_1) and PLRS image based processing for II(a) $[L/D] = [2.0, 4.0]$ and II(b) $[L/D] = 6$. The dashed black lines represent the Rossiter modes obtained using the semiempirical relation [Eq. (1)].

considered [see Fig. 7(c)], and the temporal variation of the light intensity is extracted from the PLRS snapshots and then subjected to the FFT procedure. Before discussing the variation in the dominant frequency, it is essential to establish that the measured unsteadiness is consistent and exhibits a dominant spectrum. The light-intensity fluctuations obtained from PLRS and the pressure fluctuations measured at the cavity center are shown in Fig. 10-I(a), for the case of $[L/D] = 4$ at $\mathrm{Re}_D = 74\,000$. The associated spectra are also presented in Fig. 10-I(b), which displays a close match between both the techniques as well as with the predicted frequency of the Rossiter mode within the measurement uncertainty. Based on the agreement, the comparative assessment of dominant frequencies obtained using both methods is plotted in Fig. 10-II(a) for $[L/D] = [2, 4]$. Irrespective of the $[L/D]$, the dominant frequency is found to be almost invariant of Re_D. Also, the frequency values obtained from the sensor-based FFT analysis and PLRS-based FFT analysis show a close agreement [see Fig. 10-II(a)]. Finally, the identified frequencies for $[L/D] = [2, 4]$ match the corresponding second ($n = 2 \rightarrow \mathrm{St}_D = 0.242$) and third ($n = 3 \rightarrow \mathrm{St}_D = 0.19$) Rossiter modes, respectively, as calculated using Eq. (1). It is also to be noted that the Rossiter formula was originally derived for a 2D cavity, and the good agreement with the present axisymmetric cavity is probably due to the relatively thin shear layer compared with the radius to the cone centerline. It is evident from Eq. (1) that the resonant frequency is inversely proportional to the cavity length. As a result for $[L/D] = 2$, the acoustic feedback time will be shorter, resulting in a higher dimensional frequency, which can also be referred from Fig. 10-II(a). Moreover, it is to be noted that the size of the wavelength of the K-H vortical structures and eventually the Rossiter mode numbers also depend on the initial momentum thickness. For a given momentum thickness, the number of vortices between the leading and trailing edge is an integer number corresponding to the Rossiter modes [49] and a longer cavity shear layer corresponds to more vortices along it and a higher Rossiter mode number. In conjunction with the high-resolution snapshots [see Fig. 6(b)], it can be deduced that for $[L/D] = 4$, the availability of longer streamwise extent enables instability growth (at higher Re_Ds), and the cavity resonance remains the driving factor, resulting in the St_D invariance of Re_D.

For the case of $[L/D] = 6$, a change in the dominant nondimensional frequency is observed as the Re_D is increased [see Fig. 10-II(b)]. Furthermore, there is a disparity between PLRS-based analysis and sensor-based FFT estimation in indicating the Re_D value at which shift in the dominant mode occurs. From the shear layer measurements through PLRS, the associated dominant St_D is seen to be increased from $\mathrm{St}_D = 0.035$ to $\mathrm{St}_D = 0.19$, and the Re_D corresponding to mode shifting is found to be $\mathrm{Re}_D \geqslant 51300$. However, the mode shifting is evident for $\mathrm{Re}_D \geqslant 38000$ from the FFT estimated at the cavity floor center (S_1). The shift in mode with Re_D is associated with the transition of the separated shear layer, which alters the effective phase relationship between the hydrodynamic and acoustic components of the feedback loop. In addition, the axisymmetric nature of the configuration introduces azimuthal effects that can further influence the coherence and modal selection. At intermediate Re_Ds, both the flapping (Rossiter first mode), dominating the low Re range, and the K-H (Rossiter fourth mode), dominating the high Re range, coexist. Therefore, at this range, the dominating spectral peak might shift owing to the probing location. The shear layer apparently contains fine-scale turbulent-like structures at higher Re_Ds [see Fig. 6-III(c) and 7(c)], in comparison to the large scale K-H vortices embedded in the laminar shear layer at intermediate Re_Ds [see Figs. 6-II(c) and 7(b)]. It is also worth noting that the St_D inferred from the PLRS imaging agrees closely with the Rossiter modes better than the pressure-based estimate. This might be due to the several reasons among which the azimuthal structure of the disturbances can be a factor which will be described later during the discussion on the $\Delta h/D$ variation. It is also worthwhile to note that the intermediate modes viz. second and third Rossiter modes may still be present for $L/D = 6$, particularly in the intermediate Re_D regime, which is discussed in the following paragraph. However, in this study, focus is toward identifying the dominant unsteadiness that governs the overall flow dynamics, therefore, Fig. 10-II(b) highlights the most energetic modes first and fourth across the Re_Ds for $L/D = 6$.

To ascertain the presence of multiple modes at intermediate Re_Ds which is the attributing factor for the disagreement between the imaging-based and sensor-based analysis, a surface plot (see Fig. 11) is prepared by extracting the power spectrum at all the spatial locations along a vertical line passing through the cavity center (see Fig. 11-I). At $\mathrm{Re}_D = 30000$ (Fig. 11-II), the spectrum at all $[y/D]$ locations within the shear layer thickness exhibits a dominant peak corresponding to the first Rossiter mode, which is in line with earlier observations. In a similar context, for $\mathrm{Re}_D = 74\,000$ (Fig. 11-IV), the high spectrum amplitude is clearly aligned with the fourth Rossiter mode, indicating the sole dominance of fine-scale structures. However, at $\mathrm{Re}_D = 51300$ (Fig. 11-III), the surface plot displays a mixture of several spectral peaks with the dominant one pertaining to $n = 1$ of Rossiter modes. To ensure the presence of wave structures pertaining to different Rossiter modes, spectra obtained at two vertical locations within the shear layer are shown in Figs. 11-III(a) and 11-III(b). In these range of intermediate range of Re_Ds, both modes (Rossiter first and fourth mode) coexist. The PLRS is sensitive to the exact location along and across the shear layer, whereas the

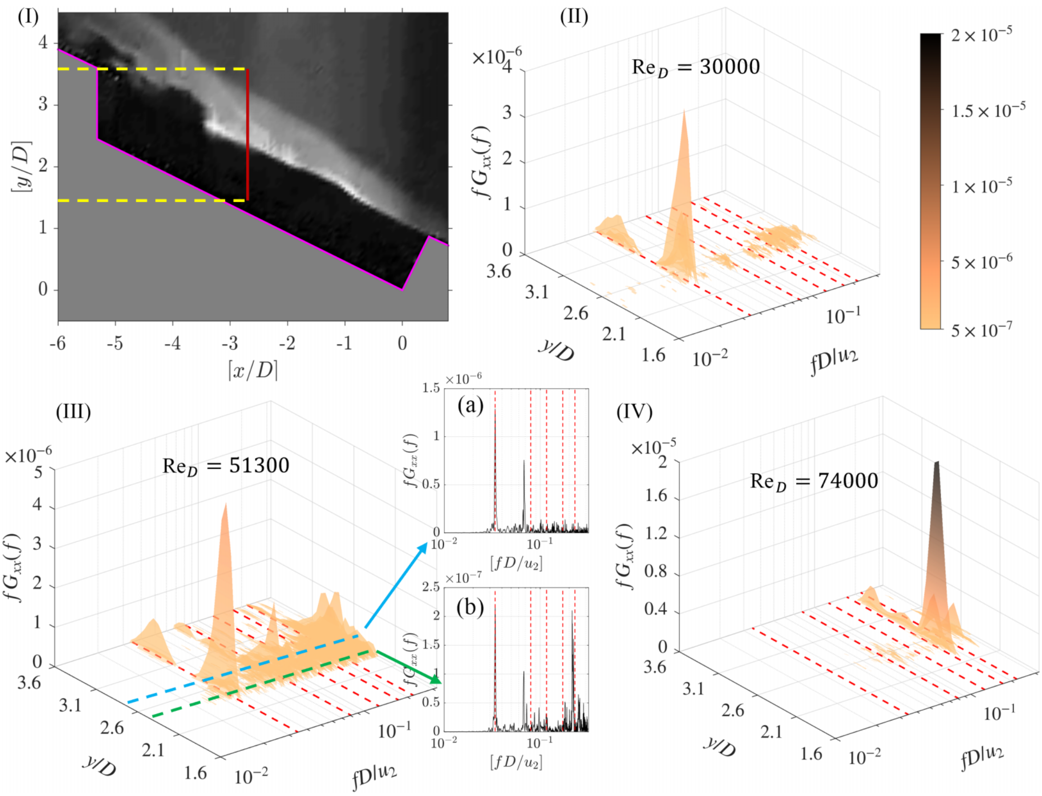

FIG. 11. (I) Representational vertical line in the cavity center marked in red color used for constructing the surface plot depicting the variation of power spectrum at different spatial locations ($[y/D]$) for (II) $\mathrm{Re}_D = 30\,000$, (III) $\mathrm{Re}_D = 51\,300$, and (IV) $\mathrm{Re}_D = 74\,000$. The red dashed lines represent different Rossiter modes. For $\mathrm{Re}_D = 51\,300$, panels (a), (b) are presented which depict the spectra at two locations within the shear layer, confirming the presence of multitude modes.

pressure sensor is not. In both cases we see the shifting of modes, but at a different Re_D. Figure 11-III shows that in these intermediate range of Re_Ds we have multiple modes, unlike the lower and higher Re_D cases, and that the peak spectra in the PLRS depend on the exact position of the measurement.

3. Dominant spatial structure estimation

Discrete spectra observed across different $[L/D]$ and Re_D combinations, as well as their association with various Rossiter modes, necessitate estimating the dominant spatial feature in each case. To estimate the spatial structures, proper orthogonal decomposition (POD) [50–52] is used in the current study. POD is primarily an energy-based decomposition to identify the dominant spatial mode from the supplied snapshot matrix. Nevertheless, the dominant mode significantly vary based on whether the subjugating matrix is embedded with the mean flow or contains a fluctuating flow field. For the present scenario, the flow is always unsteady irrespective of the shear layer characteristics viz. laminar with weakened K-H vortices or amplified K-H instabilities or transitional, as identified from the qualitative visualization. As the present investigation is centered around capturing the coherent structures dominating the flow, time-averaged-mean subtracted snapshot matrix is used. The instantaneous high-speed PLRS images acquired during the test time are used for this analysis, where each snapshot is arranged as a column of a data matrix (X), from which the temporal mean is subtracted to obtain the fluctuation matrix (X_1). The covariance matrix ($C = X_1^T X_1$) was then formed

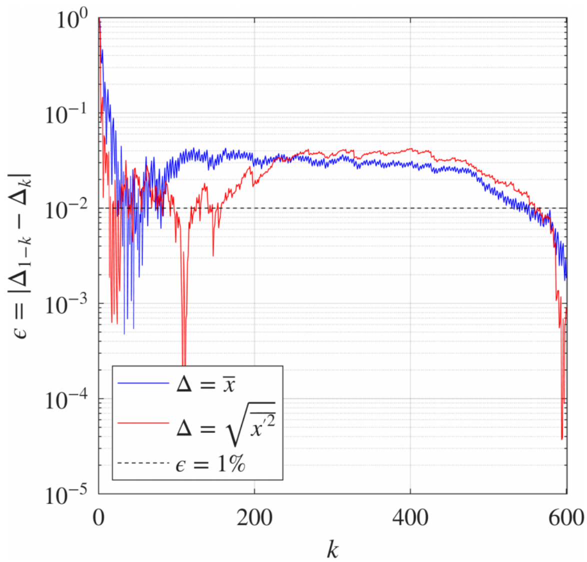

FIG. 12. Variation of mean and fluctuation rms of the light intensity with number of snapshots for the case of $[L/D] = 4$ and $\mathrm{Re}_D = 74\,000$.

and its eigenvalues (λ_i) and eigenvectors (v_i) computed via eigen decomposition ($Cv_i = \lambda_i v_i$). The eigenvalues sorted in descending order were then used to determine the cumulative energy distribution across modes, while the spatial modes (ψ_i) were obtained by projecting the eigenvectors onto the fluctuation data and normalizing the same ($\psi_i = X_1 v_i / \|X_1 v_i\|$). To arrive at a minimum number of snapshots (k) required to achieve a reasonably invariant POD mode shapes, statistical convergence study is carried out. The mean and fluctuation rms of the light intensity variation were evaluated as first and second order statistical measures, respectively, using progressively increasing k, as depicted in Fig. 12. The convergence criteria was kept in such a way that the variations observed in the averaged quantities will be less than 1% as the total number of samples considered for the analysis increases. The convergence characteristics indicate that approximately 530 and 570 images are sufficient for convergence of the mean, and fluctuation rms field, respectively. Based on this analysis, 600 instantaneous PLRS snapshots are used, ensuring statistically converged mean and fluctuation rms characteristics, and consequently reasonably invariant POD mode shapes.

The cumulative energy trend (Fig. 13-I) seems to be linearly increasing for the $[L/D] = 2$, whereas quasi-exponentially for $[L/D] = [4, 6]$, thereby indicating a significant contribution from the dominant modes. It is also clear that the associated energy level for the first dominant mode is $\approx$25% for higher $[L/D]$s, whereas 13% for $[L/D] = 2$. For $[L/D] = 2$, as the separated shear layer is mostly laminar as identified from the PLRS imaging, with very low amplitude K-H vortices embedded within it, which led to an almost linear increment in the energy content, with the requirement of a significantly higher number of modes to represent 60% of the total energy content. However, to represent 60% of the total flow energy, only 3 modes are required for $[L/D] = 4$, whereas 4 modes are essential for $[L/D] = 6$. Due to the shear layer breakdown to turbulence at $[L/D, \mathrm{Re}_D] = [6, 74\,000]$ as seen in Fig. 6-III(c), the fine-scale structures might have led to a lower slope for the increase in the cumulative energy.

The dominant spatial mode obtained through eigenvectors projection for different $[L/D]$ is presented in Figs. 13-II and 13-III(c). It is evident that irrespective of $[L/D]$ at $\mathrm{Re}_D = 74\,000$, the dominant mode consists of K-H vortices convecting along the shear layer, where alternate red and blue patches represent the streamwise wavelength of the convective structures. It is also clear that for $[L/D] = [2, 4, 6]$ the number of K-H vortices required to cover the entire length of the

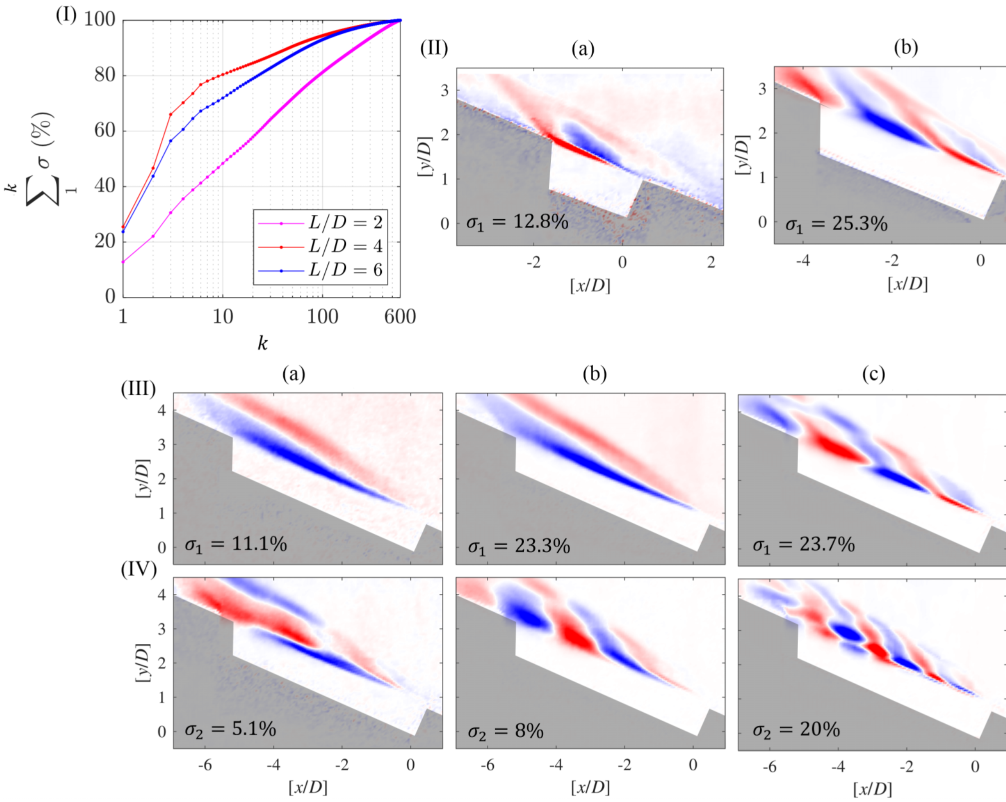

FIG. 13. (I) Variation of cumulative energy content obtained from POD analysis for different $[L/D]$ at $\mathrm{Re}_D = 74\,000$. k represents the number of instantaneous images that are used for getting the dominant modes, which is 600 for the present case. σ is representational of the associated energy content arranged in descending order. (II) Dominant spatial modes obtained through POD for (a) $[L/D] = 2$, (b) $[L/D] = 4$. σ_1 represents the energy content of the dominant mode for the respective $[L/D]$. Leading (III) first, and (IV) second POD modes representational of the overall flow for $[L/D] = 6$ at different Re_D of (a) 30 000, (b) 51 300, and (c) 74 000. Modal energy fractions σ_1 and σ_2 are indicated in each of the spatial modes.

cavity is estimated to be 2, 3, and 4, respectively. The number of structures is also representative of the Rossiter mode expected to dominate the flow. This is in line with the earlier discussion (see Sec. III A 2) that for $[L/D] = [2, 4]$, the dominant discrete frequency in the spectra is closer to the second and third Rossiter mode, respectively, and shifts to the fourth Rossiter mode for $[L/D] = 6$.

It is pertinent to note that on a similar line of observations as earlier analysis [Fig. 10-II(b)], the dominant and secondary modes (Figs. 13-III and 13-IV) clearly reveal a Re_D dependence for the case of $[L/D] = 6$. To highlight the flow structure difference, POD modes are displayed for the same three Re_D cases presented in Figs. 11-II and 11-IV. At $\mathrm{Re}_D = 30\,000$ [Fig. 13-III(a)], owing to mostly dominance of the laminar shear layer with minimal perturbation from the acoustic-hydrodynamic feedback loop as corroborated from PLRS image [see Fig. 7(a)], the low amplitude flapping of the entire shear layer having 11% of the flow energy is found to be the mode driving the flow. The second dominant mode [Fig. 13-IV(a)], with 5% of the energy, seems to be the harmonic mode of the weak shear layer flapping. So, it can be inferred that the identification of discrete frequency pertaining to the first Rossiter mode (Fig. 11-II) during the spectral analysis (see Sec. III A 2), corresponds to the entire shear layer lift-up due to the acoustic feedback loop. At $\mathrm{Re}_D = 51300$ [Fig. 13-III(b)], the energy associated with the first mode nearly doubles to 23%,

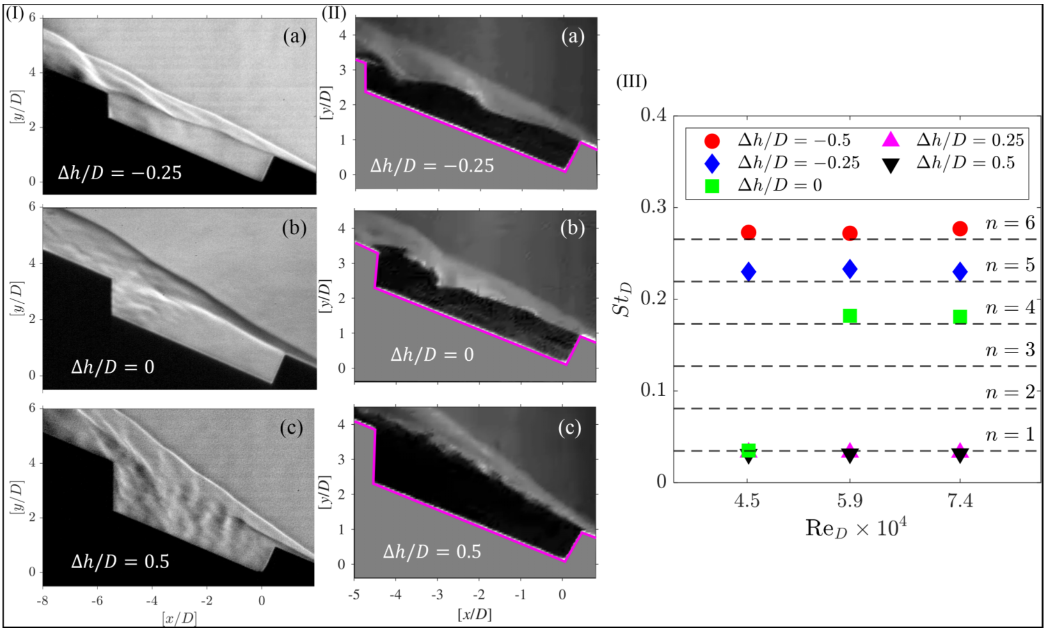

FIG. 14. Instantaneous (I) high-resolution schlieren and (II) PLRS snapshots highlighting the overall flow field for (a) $[\Delta h/D] = -0.25$, (b) $[\Delta h/D] = 0$, and (c) $[\Delta h/D] = 0.5$ at $\mathrm{Re}_D = 74\,000$. (III) Variation of St_D with change in Re_D across different cases of $[\Delta h/D]$ cases. The dashed horizontal lines correspond to Rossiter modes for $n = [1, 2, ..., 6]$ as calculated using Eq. (1) and properties mentioned in Table I. See the Supplemental Material [57] for the corresponding video files.

while still showing the shear layer lift-up as the dominant spatial feature, indicating amplified shear layer-acoustic wave interaction which is similar to flapping motion seen in leading-edge separated flows [41]. However, the second dominant mode [Fig. 13-IV(b)], accounting for 8% of the energy, consists of alternating compression and rarefaction waves, a typical signature of the K-H instability. These two modes also establish the presence of multiple mode structures with significant energy content in the shear layer in line with earlier observations (Fig. 11-III). At $\mathrm{Re}_D = 74\,000$ [Fig. 13-III(c)], the POD distribution shows a qualitative shift, with K-H vortices having ≈24% of the energy as the dominant mode, indicating the convection of instability waves driving the flow. Nevertheless, smaller scale of higher harmonics, having larger wave number structures with similar energy content (20%) is perceived as the second dominant mode [Fig. 13-IV(c)]. Overall, the POD modes while increasing Re_D for $[L/D] = 6$, collectively demonstrate the strengthening of shear layer instability equivalent to flapping through amplified acoustic-hydrodynamic coupling, followed by shifting to K-H instability and eventually introduce finer-scale transitional structures.

B. Effect of cavity's excess rear face height $[\Delta h/D]$

Experiments are conducted for $[L/D] = 6$ at specific $\mathrm{Re}_D = [45\,000, 59\,000, 74\,000]$ (refer to Fig. 14-III), across different $[\Delta h/D]$s ranging from -0.5 to 0.5 in an interval of 0.25. PLRS is performed for all the cases, and the temporal variation in light intensity is extracted at the intersection point of the shear layer and the cavity center line. Afterwards, the FFT is performed to extract the spectral content, and the dominant frequency for each case is noted. The variation of the dominant frequency in terms of St_D is obtained and compared with different Rossiter modes as shown in Fig. 14-III. It is evident that there is a change in flow interaction mechanism for $[\Delta h/D] = 0$ as the dominant mode shifts with Re_D, which has been discussed in the previous

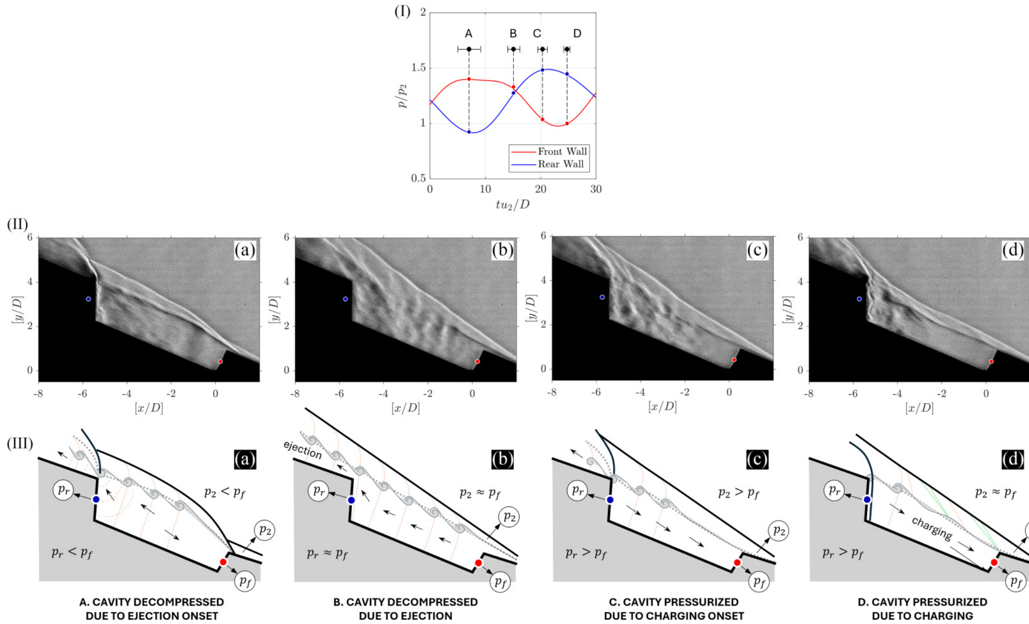

FIG. 15. (I) The pressure trace obtained from the front (p_f) and rear pressure sensor (p_r) for one breathing cycle of flapping motion depicted for the case of $[\Delta h/D] = 0.5$ at $\mathrm{Re}_D = 74\,000$. The flapping cycle is split into four representative frames (A–D) that are presented in terms of (II) instantaneous schlieren snapshots, and (III) schematic explaining the underlying flow scenario. The expected pressure at p_f and p_r during each of the frames are marked in the (I). In the schematic, flow features such as leading-edge shock, impingement shock, separation shock are marked in dark black color, with weak shocklets and acoustic waves marked in dashed orange color, and expansion fan in green color

section. For the negative cases of $[\Delta h/D]$, the shear layer is comprised of convective K-H vortices [see Figs. 14-I and 14-II(a) for $[\Delta h/D] = -0.25$), thereby indicating the same mechanism for $[\Delta h/D] = [-0.25, -0.5]$. Further, in the case of positive cases of $[\Delta h/D]$, the dominant mode number is found to be invariant across Re_D. Nevertheless, upon analysis through POD, it is observed that for $[\Delta h/D] = 0.25$ [see Fig. 17(b)], the energy content spans both mode numbers $n = 1$ and $n = 4$, with a significant contribution from the former. However, for $[\Delta h/D] = 0.5$, no spatial structure is seen convecting along the shear layer which is affirmed by the instantaneous images (see Figs. 14-I and 14-II(c) and corresponding videos in the Supplemental Material [57]). As the present study attempts to investigate the flow evolution across different standalone flow scenarios, we shall concentrate on cases having one type of dominant spatial mode ($[\Delta h/D] = [-0.25, 0.5]$) while varying $[\Delta h/D]$.

The instantaneous schlieren images are captured at a higher frequency (sampling rate of 52 kHz) only for the cases of $[\Delta h/D] = 0.5$ and $\mathrm{Re}_D = 74\,000$, to better understand the underlying mechanism driving the unsteadiness. Simultaneously, pressure responses at the front (p_f) and trailing edge (p_r) of the cavity are also acquired to correlate the events with the schlieren snapshots. As a whole, K-H vortices convecting along the shear layer without lift-up are observed for $[\Delta h/D] = -0.25$, similar to characteristics of a regular open cavity configuration. However, the entire shear layer and shock system is seen to be flapping for the case of $[\Delta h/D] = 0.5$. For one cycle of flapping, the typical pressure response obtained from the front and rear sensors for $[\Delta h/D] = 0.5$ is shown in Fig. 15-I. The relevant schlieren frames (A–D) necessary to explain one flapping cycle are shown in Fig. 15-II, along with the associated pressure magnitudes marked in Fig. 15-I. Also, for better clarity, the corresponding simplified schematic depicting the wave diagram in line with the instantaneous schlieren snippet is shown in Fig. 15-III. The pressure traces, in conjunction with the schlieren frames, indicate that the $[\Delta h/D] = 0.5$ case undergoes a distinct breathing cycle driven by alternating under- and over-expansion. To isolate the events, it is split into four frames, presented in Figs. 15-II and 15-III. Frame A (Fig. 15-II) shows the flowfield close to the onset of depressurization of the cavity demarcated by shear layer lift-up near the leading edge. The pressure imbalance, with higher pressure in the vicinity of the front wall than the rear wall ($p_f > p_r$), has resulted in a strong upward motion of the shear layer and local over-expansion near the lip of the cavity leading edge ($p_f > p_2$). The cavity trailing zone appears to be filled with fine ripples and tiny compressed spots, representing acoustic waves and weak shocklets. As the cavity begins to transition from its previously compressed state, the rear region relaxes through weaker pressure pulses and acoustic waves. Also, the increased front-face pressure (p_f) at the cavity lip results in upstream motion of the shear layer and separation shock, which is evident in Frame B of Fig. 15-II.

The venting process continues from Frame A to B, where Frame B represents a flow situation where the separation shock reaches its extreme extent, resulting in pressure equalization of the cavity interior with the freestream flow ($p_f \approx p_r \approx p_2$). With the shear layer no longer supported by excess front pressure, the external supersonic flow begins to push the shock and shear layer downward. The downward motion is initiated by admitting a small amount of high-speed flow back into the cavity through the first set of weak compression waves, as can be clearly seen in Frame B of Fig. 15-II. With further leaning of the shear layer toward the cavity, high-speed outer flow entrains into the cavity before reaching a stable configuration where the shear layer strikes the rear wall, resulting in a strong impingement shock (see Frame C in Fig. 15-II), which is also the onset of the recompression phase of the cavity. Frame C shows a streak of thin, oblique, high-contrast density-gradient bands along and above the shear layer near the trailing edge. Following the nomenclature commonly used in compressible flow literature [53,54], these structures are referred as shocklets, viz. weak compression fronts associated with locally supersonic convecting vortical shear layer structures. The appearance of shocklets is accompanied by the strong rear wall impingement of the downward deflected shear layer and the associated rise in p_r. In the mean time, also the forcing from the freestream flow pushes the shear layer fully downward and locking at its maximum inward curvature, with the presence of a centered expansion fan around the leading edge lip of the cavity, as seen in Frame D of Fig. 15-III. Also, the impingement shock has grown into a steep, anchored shock with its foot on the cavity floor, indicating that high-momentum outer flow is being injected into the cavity, resulting in a continuous pressurization, which, at a later time, pushes the shear layer upward, thereby completing the cycle. Furthermore, the mean pressure is measured across several runs and oscillation cycles at the p_f and p_r locations, which results in a pressure gradient of $dp/dx = ((\overline{p_f} - \overline{p_r})/p_2)/(L/D)$ of 0.0323, indicating the intermittent excess pressure at the front face causing the upward movement of the shear layer near the leading edge that drives the overall unsteadiness.

The instantaneous schlieren snapshots for $[\Delta h/D] = -0.25$ at $\mathrm{Re}_D = 74\,000$ [see Figs. 14-I and 14-II(a)], reveal a shear layer with the presence of less intense K-H vortices and the associated weak shocklets within the shear layer. The shear layer impingement consistently overshoots the rear lip, reattaching downstream of the trailing edge with embedded K-H vortices, confirming that the shear layer is mainly governed by the convective instability, unlike the pressure build-up for $[\Delta h/D] = 0.5$. Also, due to the shear layer impingement downstream of the rear face, only weak perturbations transmit into the cavity, thereby helping in prohibiting the triggering of transition as seen in $[\Delta h/D] = 0$ [see Figs. 14-I and 14-II(b)]. Also, the shear layer seems to support smaller-wavelength vortical structures owing to a longer shear layer path and a weaker pressure-feedback loop. The pressure gradient across the leading and trailing edges measured from the p_f and p_r sensors is calculated to be -0.0033, one order of magnitude lower than the case of $[\Delta h/D] = 0.5$. The relatively weaker K-H vortices convecting downstream shed weaker compression waves, which are felt mainly by the p_r sensor. Since the cavity-driven resonance is weaker, the overall cavity pressure remains low, and the downstream convective vortices naturally produces marginally higher p_r than p_f. The normalized mean pressure inside the cavity ($\zeta = \overline{p}/p_2$) during the test duration

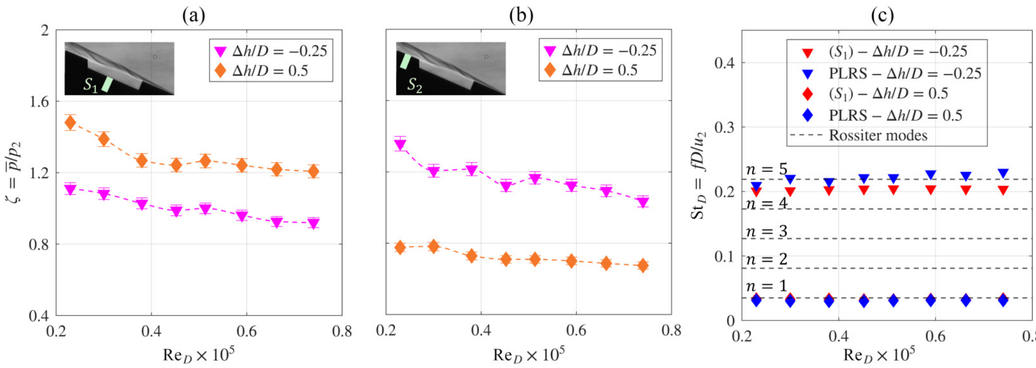

FIG. 16. Nondimensional mean pressure variation at the (a) cavity floor center, S_1, and (b) cavity downstream, S_2, location with change in $[\Delta h/D]$ and Re_D at $[L/D] = 6$. (c) Comparison of dominant frequency obtained from the sensor (S_1) and PLRS image based processing with change in Re_D for $[\Delta h/D] = [-0.25, 0.5]$.

is measured from the response of S_1. The value of ζ for $[\Delta h/D] = 0.5$ is found to be higher than that of the $[\Delta h/D] = -0.25$, irrespective of the Re_D [see Fig. 16(a)]. The significant increase in ζ corresponds to distinct patterns of flow unsteadiness observed during the schlieren imaging reported previously. The case of $[\Delta h/D] = 0.5$ pertains to a situation where the entire shock and shear layer system flap severely, thereby imparting a higher cyclic load on the cavity, similar to leading-edge-separated flows [41]. However, for $[\Delta h/D] = -0.25$, the separated shear layer is perturbed by the K-H instability structures spanning the entire cavity [see Fig. 14-I and 14-II(a)], resulting in a lesser pressure loading. Comparing Figs. 16(a) and 16(b), the flapping mode is found exerting higher pressure inside the cavity (S_1), while the K-H mode on the downstream cavity location (S_2). The impingement of the shear layer downstream of the trailing edge for $[\Delta h/D] = -0.25$ causes higher pressure for the cavity location S_2. Also, owing to the cavity breathing motion seen for $[\Delta h/D] = 0.5$, the impingement shock strength varies intermittently, to ensure flow relaxation, leading to a lesser pressure rise at the downstream location. Nevertheless, the trend of decrement in ζ with increase in Re_D is common for both the inside and downstream of the cavity cases (see Fig. 16).

The dominant frequency obtained from the sensor (S_1) and the PLRS-based FFT analysis for two $[\Delta h/D]$ cases is shown in Fig. 16(c). For $[\Delta h/D] = 0.5$, the dominant St_D is quantified as 0.036, which is the same as observed during the postprocessing of the high-repetition-rate PLRS imaging. Also, this nondimensional frequency matches with the first Rossiter mode obtained from Eq. (1) for $[L/D] = 6$. Similarly, for $[\Delta h/D] = -0.25$, the dominant nondimensional frequency is found to be $[fD/u_2] = 0.2$, which has a slight deviation from the values obtained from the PLRS-based imaging ($[fD/u_2] = 0.21$). Moreover, these values are closer to Rossiter's fifth mode ($[fD/u_2] = 0.217$). For both the cases of $[\Delta h/D] = -0.25, 0.5$, the dominant frequency is found to be invariant of Re_D.

With the same analogy as $[L/D]$ variation, 600 PLRS frames during the steady test duration are subjected to POD toward extracting the dominant spatial mode driving the flow. The identified spatial modes are displayed in Figs. 17(a) and 17(c) for $[\Delta h/D] = -0.25, 0.5$, respectively. In line with observation of weaker K-H vortices along the shear layer in the schlieren snapshots, the dominant mode is also found to have 19% energy [see Fig. 17-I(a)] in comparison to 24% energy for the case of $[\Delta h/D] = 0$ [see Fig. 13-III(c)]. Both the first and second dominant energetic modes for $[\Delta h/D] = -0.25$ establish the presence of K-H vortices in the shear layer through alternating red and blue patches with a phase shift for the secondary mode. Also, the number of vortices spanning the cavity reaffirms the match between the dominant frequency and the fifth Rossiter mode. Together, the spatial modes indicate the significance of convective-dominated shear layer

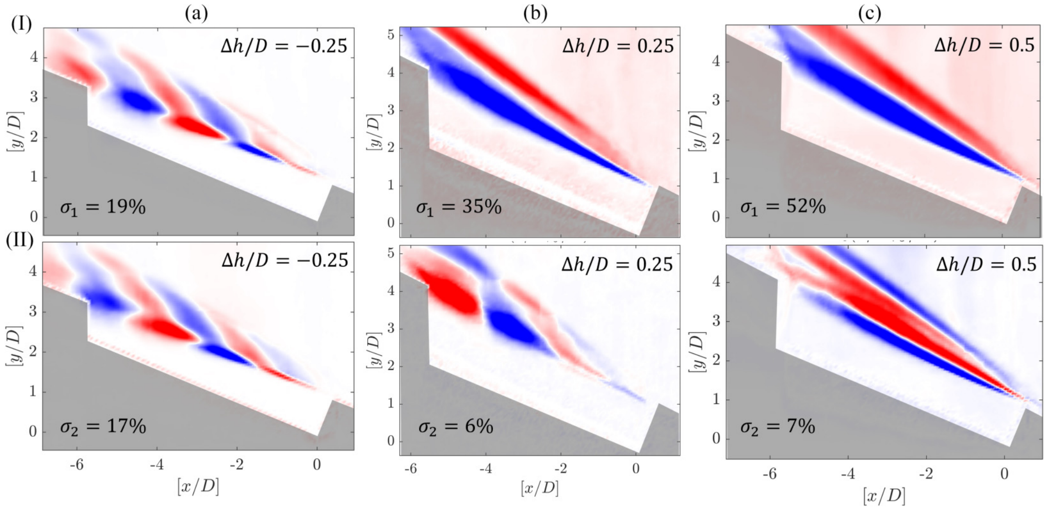

FIG. 17. Spatial structure corresponding to the dominant (I) first and (II) second mode obtained through POD analysis for $[L/D] = 6$ at different $[\Delta h/D]$ of (a) -0.25, (b) 0.25, and (c) 0.5. σ represents the respective model energy content.

toward driving the overall flow. In contrast, the first dominant mode for $[\Delta h/D] = 0.5$ constitutes 52% of the total flow energy [see Fig. 17-I(c)], signifying the large-scale pressure-driven motion resulting in bulk vertical displacement of the entire shear layer. A similar flow pattern has also been reported in leading-edge separated flows [41]. The strong intensity of the most energetic mode indicates that the cavity behaves like a single low-frequency oscillating fluid volume. The secondary mode [see Fig. 17-II(c)] seems to be a complementary phase of the coherent vertical displacement of the shear layer. The quantitative signature of the breathing mechanism matches the frequency associated with the first Rossiter mode.

With variation of $[\Delta h/D]$, two different spatial flow patterns dominating the flow and leading to unsteadiness are evident. To determine the azimuthal nature of these oscillations, four pressure probes equally spaced are placed along the circumferential direction [see Fig. 18(a)]. Experiments

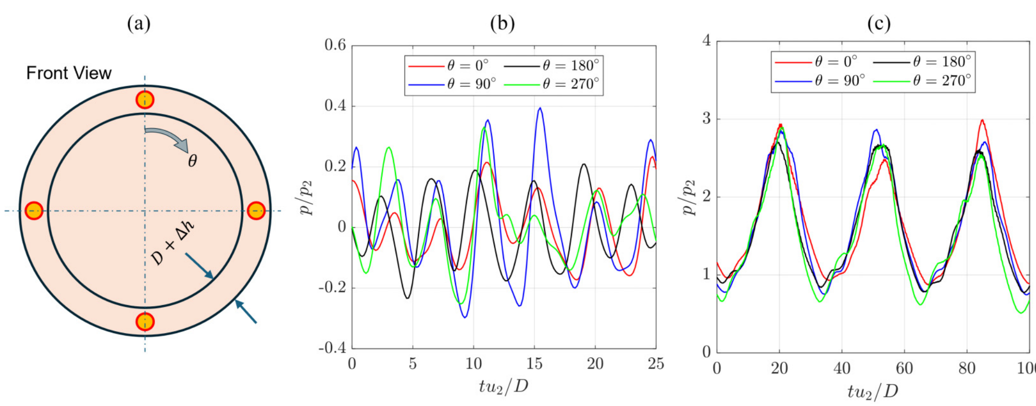

FIG. 18. (a) Locations of the sensor's placement along the azimuthal direction on the rear face of the cavity. The pressure responses obtained from these sensors are plotted for the case of (b)$[\Delta h/D] = -0.25$ and (c) $[\Delta h/D] = 0.5$, depicting no clear corelation for $[\Delta h/D] = -0.25$, and coherent signals for $[\Delta h/D] = 0.5$.

are performed for the two representative cases of $[\Delta h/D] = [-0.25, 0.5]$, at a freestream $\mathrm{Re}_D =$ 74 000. The responses obtained from the sensors in the case of $[\Delta h/D] = -0.25$ are shown in Fig. 18(b), from which a clear difference in amplitude and phase among all the azimuthal locations is evident. However, for the case of $[\Delta h/D] = 0.5$, the pressure fluctuations across all the azimuthal locations exhibit near identical amplitudes without any significant phase delay [see Fig. 18(c)], confirming that the flapping mode is axisymmetric.

To further quantify the azimuthal behavior, modal decomposition from the acquired responses is carried out for the respective dominant Rossiter frequency (f_0) using the approach described by Cohen and Wygnanski in Sec. 2.2 of Ref. [55]. This allows the separation of the amplitude at f_0 into axisymmetric (denoted by $m = 0$) and the first azimuthal component (denoted by $m = \pm 1$), which are also representative of forward- and backward-rotating modes. The modal separation for $[\Delta h/D] = -0.25$ (K-H mode) resulted in amplitudes of $m = 0,\ +1$, and -1 as $0.053,\ 0.046$, and 0.031, respectively, which are small and comparable in magnitude without any preferential direction of propagation. It is also to be noted that any specific corelation could not be established among the sensors which is in agreement with findings reported by Creighton and Hillier [39]. Similarly, for the $[\Delta h/D] = 0.5$ (flapping mode), the modal separation results in amplitudes of $m = 0,\ +1$, and -1 as $0.6,\ 0.044$, and 0.038, respectively. The dominance of the axisymmetric mode in comparison to the helical modes establishes the azimuthal uniformity of the flow features for the case of $[\Delta h/D] = 0.5$.

C. Flow disparity between two-dimensional and axisymmetric cavities

The following section highlights the differences in flow evolution between axisymmetric and two-dimensional cavities across the Re_D range for $[L/D] = 6$. In this regard, a two-dimensional cavity configuration in the form of a rectangular groove is made on a wedge having a semiapex angle of 20.5°. Upon exposure to the freestream flow of $M_\infty = 6.0$, an oblique shock is formed at the leading edge of the wedge, resulting in a cavity upstream Mach number, $M_2 = 3.32$. Flow conditions downstream of the oblique shock remain almost the same as those of downstream of the conical shock in the axisymmetric cavity case, as shown in Table I. The width of the wedge is $w/D = 10$, with side plates installed to prevent sideward flow spillage. The cavity leading edge is located at a slant distance of $L_F = 3.6D$ from the wedge tip, the same as for the axisymmetric counterpart; therefore, the incoming boundary layer thickness and the respective Re_x across different fill conditions can be assumed to be the same. Experiments are performed for p_0 ranging between 3 to 10 bar, resulting in Re_D of 23 000 and 74 000 for the extreme cases of operation. High-repetition-rate PLRS imaging is performed to capture flow evolution in the cavity center plane, with a spatial resolution of 128×96 pixels at an acquisition rate of 100 kHz. The temporal variation of light intensity is extracted at the shear layer midpoint, and a further FFT is performed to identify the dominant frequency. The comparison of dominant frequency across the Re_D cases for both the axisymmetric and two-dimensional cavity configurations is depicted in Fig. 19-I. It is clearly evident that the dominant frequency matches with the fourth Rossiter mode for all the Re_Ds in the 2D cavity, demonstrating the Re_D independence of the dominant frequency, in agreement with earlier studies [20,56], in contrast to the shift in dominant behavior from first to fourth Rossiter mode observed for the axisymmetric cavities.

Further, to have a quantitative comparison on the shear layer perturbation location for the two-dimensional configuration, s-f plots are generated as shown in Fig. 19-II. Much like the dominant frequency, the perturbation onset along the shear layer is also found to be constant ($s/D = 1.05$), which demarcates the coherence of the separated shear layer across the Re_D cases. This is again in contrast to the axisymmetric cavity case, where upstream movement of the perturbation location is seen with increases in Re_D (see Fig. 8), which further results in shear layer breakdown owing to longer propagation length from the perturbed location to the trailing edge. Moreover, the instantaneous PLRS images are subjugated through the POD technique to arrive at the dominant mode, which is presented in Fig. 19-III. All the Re_D cases display convecting K-H

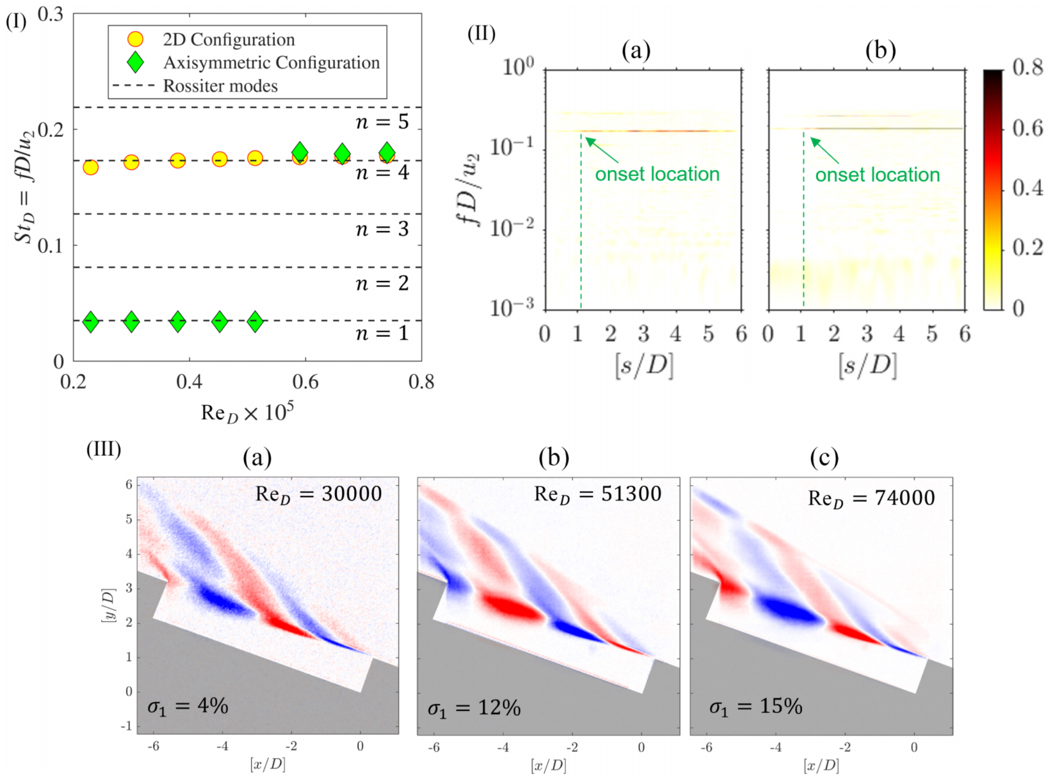

FIG. 19. (I) Comparison of the dominant frequency obtained from the PLRS image based processing for the two-dimensional and axisymmetric cavity configuration for $[L/D] = 6$. The dashed black lines represent the Rossiter modes obtained using the semiempirical relation as mentioned in Eq. (1). (II) s-f diagram generated for the case of two-dimensional cavity configuration having $[L/D] = 6$ at (a) $Re_D = 23\,000$ and (b) $Re_D = 74\,000$ where the profile is generated along the shear layer. A representative line along which s-f plot is generated, is marked in dashed green color in Fig. 7(b). (III) Dominant spatial structure obtained through POD analysis for two-dimensional cavity having $[L/D] = 6$ at different Re_D of (a) 30 000, (b) 51 300, and (c) 74 000. See the Supplemental Material [57] for the corresponding video files.

vortices of identical characteristic wavelength that extend from the leading edge to the trailing edge, thereby establishing the invariant of the dominant St_D in line with PLRS-based spectral analysis (see Fig. 19-I). With increases in Re_D, the amplification of instability wave occurs [compare Figs. 19-III(a) and 19-III(c)] without altering the underlying topology of the coherent structures, thereby confirming that irrespective of the Re_D, the dominant dynamics are driven by the same Rossiter-type shear layer instability. Nevertheless, the axisymmetric cavity at lower Re_Ds [see Fig. 13-III(a)] is found to be driven by the shear layer lift-up (Rossiter first mode), which intensifies at intermediate Re_Ds [see Fig. 13-III(b)] along with significant contribution from the Rossiter fourth mode [see Fig. 13-IV(b)]. Finally, at higher Re_Ds [see Fig. 13-III(c)], K-H vortices, along with fine-scale turbulent structures resulted out of shear layer transition to turbulence, is seen to be dominating the overall flow field.

IV. SUMMARY AND CONCLUSIONS

Experiments to understand the shear layer characteristics and identify the source of unsteadiness during hypersonic flow over axisymmetric cavities mounted on a cone are performed using the HLT located at Technion. Various cavity geometries with different aspect ratios ($[L/D] = [2,\ 4,\ 6]$) are exposed to hypersonic flow having a freestream Mach number $M_\infty = 6.0$, at a wide range of Reynolds numbers ($23\,000 \leqslant \mathrm{Re}_D \leqslant 74\,000$). Additionally, the effect of varying the shear layer reattachment location through normalized excess height of the rear face ($[\Delta h/D] = [-0.5, -0.25, 0, 0.25, 0.5]$) is also assessed for $[L/D] = 6$. High-resolution schlieren snapshots reveal the overall flow features, including the leading-edge shock, the separated shear layer, K-H vortices, and the reattachment shock. Similarly, high-repetition-rate PLRS imaging is used to construct space-time (x-t) and space-frequency (x-f) plots to establish the unsteadiness level for different cases. Along with the qualitative interpretation, quantitative estimates are obtained using pressure probes at different locations, enabling identification of the mean pressure variation and the dominant frequency through FFT.

(1) *Effects of length to depth ratio* ($[L/D]$). Increasing $[L/D]$ fundamentally alters the shear layer dynamics through amplifying instability and strengthening acoustic-hydrodynamic coupling. For a relatively short cavity ($[L/D] = 2$), the schlieren and PLRS snapshots reveal a predominantly laminar shear layer with lesser intense K-H vortices convecting at a frequency that matches the second Rossiter mode, which is also evident from the POD analysis that shows one set of alternate colored-lobes that span the entire cavity length. The pressure response within and downstream of the cavity is nearly identical, indicating a stable recirculation region. For $[L/D] = 4$, visible K-H vortices with intensified fluctuation levels and a reattachment shock with increase in Re_D are observed from the qualitative imaging, which, upon analysis, shows Reynolds number independent behavior for St_D that matches the third Rossiter mode, along with a modest pressure variation between the cavity center and downstream location. For a relatively longer cavity ($[L/D] = 6$), the shear layer becomes highly receptive, with the associated perturbation location shifting upstream as Re_D increases, resulting in transition to turbulence owing to longer traverse length for the shear layer accompanied by amplified K-H instabilities. At intermediate Re_Ds, both, the flapping ($n = 1$), dominating the low Re_D range, and the K-H ($n = 4$), dominating the high Re_D range, coexist. Therefore, at this range, the dominant spectral peak detected by the sensor, might depend on its location. It should be noted that the K-H mode is observed to prevail throughout the entire Re_D range in the two-dimensional cavity case under the same flow conditions. The pressure measurement at the cavity center approaches the freestream value as the shear layer transitions to turbulence. The latter also results in $\approx$20% lower pressure at the downstream reattachment location. For $[L/D] = 6$, POD analysis suggests that for the shear layer, the lift-up is similar to the flapping behavior at lower Re_Ds, and that the K-H vortices of different wave number dominate the flow at higher Re_Ds.

(2) *Effects of excess rear face height to depth ratio* ($[\Delta h/D]$). For the negative excess rear face height to depth ratio ($[\Delta h/D] = -0.25$), schlieren images display K-H vortices convecting downstream without appreciable lift-up, and the reattachment shock constantly overshoots the trailing edge, resulting in a relatively weakly forced shear layer scenario and a minimal pressure gradient along the cavity. POD analysis also establishes the dominance of K-H vortices with associated frequency matching the fifth Rossiter mode. In contrast, for the positive excess rear face height to depth ratio ($[\Delta h/D] = 0.5$), schlieren revealed a pronounced flapping of the shear layer, for which the St_D matches the first Rossiter mode across all the Re_D cases. The flapping mode is similar to the shock-shear layer oscillation observed in leading-edge separated flows. One cycle of the cavity breathing motion is prompted by the alternate under- and overexpansion process. This involves the shear lift-up together with upstream movement, depressurization of the cavity, leading to the maximum extent of the shock-shear layer system. The latter events are followed by the cavity pressurization induced by the strong impingement shock having a foot on the cavity floor, as well as the presence of shocklets near the trailing edge. POD for $[\Delta h/D] = 0.5$ also indicates the presence of a single strongly coupled resonant structure spanning across the cavity length as the dominant one. For the positive excess rear face height to depth ratio, strong flapping results in higher pressure within the cavity, whereas for the negative excess rear face height to depth ratio, downstream impingement of the shear layer leads to higher pressure at the postcavity

location. Azimuthal pressure variation on the cavity rear face and further postprocessing via mode separation indicate the axisymmetric nature of the flapping mode, whereas K-H vortices did not show significant correlated behavior.

ACKNOWLEDGMENTS

The authors gratefully acknowledge the invaluable contributions of the late Mark Koifman, Lab Chief Engineer, Technion Wind Tunnel Complex, whose engineering vision was instrumental in the realization of the Hypersonic Ludwieg Tunnel (HLT) at Technion. His efforts made this experimental work possible. The authors also thank the other engineers, including M. Dunaevsky, O. Kan, N. Shefer, D. Naftali, and E. Shulman, for their significant assistance in conducting these challenging experiments.

DATA AVAILABILITY

The data that support the findings of this study are available from the corresponding author upon reasonable request. The data are not publicly available due to their large size and/or institutional storage limitations.

[1] S. J. Beresh, J. L. Wagner, and K. M. Casper, Compressibility effects in the shear layer over a rectangular cavity, J. Fluid Mech. **808**, 116 (2016).

[2] Y. P. Guo, K. J. Yamamoto, and R. W. Stoker, Experimental study on aircraft landing gear noise, J. Aircr. **43**, 306 (2006).

[3] G. Robertson and R. Kumar, Effects of a generic store on cavity resonance at supersonic speeds, AIAA J. **58**, 4426 (2020).

[4] S. J. Lawson and G. N. Barakos, Computational fluid dynamics analyses of flow over weapons-bay geometries, J. Aircr. **47**, 1605 (2010).

[5] S. H. Kang, Y. J. Lee, S. S. Yang, M. K. Smart, and M. V. Suraweera, Cowl and cavity effects on mixing and combustion in scramjet engines, J. Propul. Power **27**, 1169 (2011).

[6] S. I. Silton and D. B. Goldstein, Use of an axial nose-tip cavity for delaying ablation onset in hypersonic flow, J. Fluid Mech. **528**, 297 (2005).

[7] A. Ben-Yakar, B. Natan, and A. Gany, Investigation of a solid fuel scramjet combustor, J. Propul. Power **14**, 447 (1998).

[8] D. Cao, H. E. Brod, N. Yokev, and D. Michaels, Flame stabilization and local combustion modes in a cavity-based scramjet using different fuel injection schemes, Combust. Flame **233**, 111562 (2021).

[9] Q. Liu, III, Y. Sun, C.-A. Yeh, L. S. Ukeiley, L. N. Cattafesta, III, and K. Taira, Unsteady control of supersonic turbulent cavity flow based on resolvent analysis, J. Fluid Mech. **925**, A5 (2021).

[10] R. C. Murray and G. S. Elliott, Characteristics of the compressible shear layer over a cavity, AIAA J. **39**, 846 (2001).

[11] M. McGilvray, P. A. Jacobs, R. G. Morgan, R. J. Gollan, and C. M. Jacobs, Helmholtz resonance of Pitot pressure measurements in impulsive hypersonic test facilities, AIAA J. **47**, 2430 (2009).

[12] T. Mathur, M. Gruber, K. Jackson, J. Donbar, W. Donaldson, T. Jackson, and F. Billig, Supersonic combustion experiments with a cavity-based fuel injector, J. Propul. Power **17**, 1305 (2001).

[13] D. R. Chapman, D. M. Kuehn, and H. K. Larson, Investigation of separated flows in supersonic and subsonic streams with emphasis on the effect of transition, Technical Report No. 1356, 1958, https://digital.library.unt.edu/ark/67531/metadc60772/.

[14] K. M. Nicoll, A study of laminar hypersonic cavity flows, AIAA J. **2**, 1535 (1964).

[15] J. L. Everhart and F. A. Greene, Turbulent supersonic/hypersonic heating correlations for open and closed cavities, J. Spacecr. Rockets **47**, 545 (2010).

[16] A. Morgenstern, Jr. and N. Chokani, Hypersonic flow past open cavities, AIAA J. **32**, 2387 (1994).
[17] J. E. Rossiter, Wind-tunnel experiments on the flow over rectangular cavities at subsonic and transonic speeds, Aeronautical Research Council Reports and Memoranda, 1964, https://reports.aerade.cranfield.ac.uk/handle/1826.2/4020.
[18] C. W. Rowley, T. Colonius, and A. J. Basu, On self-sustained oscillations in two-dimensional compressible flow over rectangular cavities, J. Fluid Mech. **455**, 315 (2002).
[19] Y. Sun, III, K. Taira, L. N. Cattafesta, III, and L. S. Ukeiley, Biglobal instabilities of compressible open-cavity flows, J. Fluid Mech. **826**, 270 (2017).
[20] H. Heller, D. Holmes, and E. Covert, Flow-induced pressure oscillations in shallow cavities, J. Sound Vib. **18**, 545 (1971).
[21] V. Thangamani, Mode behavior in supersonic cavity flows, AIAA J. **57**, 3410 (2019).
[22] C. Zhang, R. Li, Z. Xi, Z. Wan, and D. Sun, Effect of Mach number on the mode transition for supersonic cavity flows, Aerosp. Sci. Technol. **106**, 106101 (2020).
[23] T. F. Rezende, F. O. Aguirre, V. B. Victorino, and M. A. Medeiros, Computational study of asymmetric gaps, in *Proceedings of the AIAA Aviation Forum and ASCEND* (American Institute of Aeronautics and Astronautics (AIAA), Virginia, 2024), p. 4487.
[24] M. S. Mathias and M. A. F. de Medeiros, The effect of Mach number on open cavity flows with thick or thin incoming boundary layers, Theor. Comput. Fluid Dyn. **35**, 495 (2021).
[25] W. Li, T. Nonomura, A. Oyama, and K. Fujii, Feedback mechanism in supersonic laminar cavity flows, AIAA J. **51**, 253 (2013).
[26] D. Papamoschou and A. Roshko, The compressible turbulent shear layer: An experimental study, J. Fluid Mech. **197**, 453 (1988).
[27] G. A. Bres and T. Colonius, Three-dimensional instabilities in compressible flow over open cavities, J. Fluid Mech. **599**, 309 (2008).
[28] N. Sandham and W. Reynolds, Three-dimensional simulations of large eddies in the compressible mixing layer, J. Fluid Mech. **224**, 133 (1991).
[29] P. S. Doshi, R. Ranjan, and D. V. Gaitonde, Global and local modal characteristics of supersonic open cavity flows, Phys. Fluids **34**, 034104 (2022).
[30] F. M. Garrido, Instability analysis of incompressible open cavity flows, Doctoral thesis, ETSIAE UPM Madrid, 2014.
[31] M. R. Islam and Y. Sun, Identification of cross-frequency interactions in compressible cavity flow using harmonic resolvent analysis, J. Fluid Mech. **1000**, A13 (2024).
[32] J. de Vicente, J. Basley, F. Meseguer-Garrido, J. Soria, and V. Theofilis, Three-dimensional instabilities over a rectangular open cavity: From linear stability analysis to experimentation, J. Fluid Mech. **748**, 189 (2014).
[33] Y. Luo, H. Tian, C. Wu, H. Li, Y. Wang, and S. Zhang, Evolution of tornado-like vortices in three-dimensional compressible rectangular cavity flows, J. Fluid Mech. **955**, A9 (2023).
[34] F. O. Aguirre, V. B. Victorino, P. C. Paino, H. Ben-Gida, and M. A. Medeiros, Mach effect on instability and transition in flows over gaps, in *Proceedings of the AIAA Aviation Forum and ASCEND* (AIAA, Las Vegas, Nevada, 2025), p. 3456.
[35] K. M. Casper, J. L. Wagner, S. J. Beresh, R. W. Spillers, J. F. Henfling, and L. J. Dechant, Spatial distribution of pressure resonance in compressible cavity flow, J. Fluid Mech. **848**, 660 (2018).
[36] J. Häberle and A. Gülhan, Investigation of two-dimensional scramjet inlet flowfield at Mach 7, J. Propul. Power **24**, 446 (2008).
[37] K. Yuceil and D. Dolling, Nose cavity effects on blunt body pressure and temperatures at Mach 5, J. Thermophys. Heat Transfer **9**, 612 (1995).
[38] A. Jackson, R. Hillier, and S. Soltani, Experimental and computational study of laminar cavity flows at hypersonic speeds, J. Fluid Mech. **427**, 329 (2001).
[39] S. Creighton and R. Hillier, Experimental and computational study of unsteady hypersonic cavity flows, Aeronaut. J. **111**, 673 (2007).
[40] P. J. Block, Noise response of cavities of varying dimensions at subsonic speeds, Technical Report, NASA Technical Note D-8351, 1976.

[41] S. Karthick, S. R. Nanda, and J. Cohen, Unsteadiness in hypersonic leading-edge separation, Exp. Fluids **64**, 13 (2023).
[42] M. Schuabb, L. Duan, K. M. Casper, R. M. Wagnild, M. M. Choudhari, and P. Paredes, Hypersonic boundary-layer transition over a circular cone in a Mach 8 digital wind tunnel, J. Fluid Mech. **1017**, A33 (2025).
[43] G. S. Settles, *Schlieren and Shadowgraph Techniques: Visualizing Phenomena in Transparent Media* (Springer Science & Business Media, Berlin, 2001).
[44] C. Zhang and C. Lee, Rayleigh-scattering visualization of the development of second-mode waves, J. Visualization **20**, 7 (2017).
[45] M. A. Trudgian, W. O. Landsberg, and A. Veeraragavan, Experimental investigation of inclining the upstream wall of a scramjet cavity, Aerosp. Sci. Technol. **99**, 105767 (2020).
[46] Y. Oka, Y. Ozawa, T. Nagata, K. Asai, and T. Nonomura, Experimental investigation of the supersonic cavity by spectral-pod of high-sampling rate pressure-sensitive paint data, Exp. Fluids **64**, 108 (2023).
[47] H. W. Coleman and W. G. Steele, *Experimentation, Validation, and Uncertainty Analysis for Engineers* (John Wiley & Sons, New York, NY, 2009).
[48] D. K. Golui, K. Noorul Ameen, and S. Desikan, Measurement uncertainty and sensitivity analyses on freestream parameters in a hypersonic impulse facility: A perturbation-based framework, Phys. Fluids **37**, 127136 (2025).
[49] C. K. Tam and P. J. Block, On the tones and pressure oscillations induced by flow over rectangular cavities, J. Fluid Mech. **89**, 373 (1978).
[50] J. L. Lumley, The structure of inhomogeneous turbulent flows, in *Atmospheric Turbulence and Radio Wave Propagation*, edited by A. M. Yaglom and V. I. Tatarsky (Nauka, Moscow, 1967), pp. 166–178.
[51] L. Sirovich, Turbulence and the dynamics of coherent structures. Part I: Coherent structures, Q. Appl. Math. **45**, 561 (1987).
[52] K. E. Meyer, J. M. Pedersen, and O. Özcan, A turbulent jet in crossflow analysed with proper orthogonal decomposition, J. Fluid Mech. **583**, 199 (2007).
[53] T. Rossmann, M. G. Mungal, and R. K. Hanson, Evolution and growth of large-scale structures in highcompressibility mixing layers, J. Turbul. **3**, N9 (2002).
[54] S. K. Lele, Compressibility effects on turbulence, Annu. Rev. Fluid Mech. **26**, 211 (1994).
[55] J. Cohen and I. Wygnanski, The evolution of instabilities in the axisymmetric jet. Part 1. The linear growth of disturbances near the nozzle, J. Fluid Mech. **176**, 191 (1987).
[56] K.-M. Chung, Y.-X. Huang, L. Kuan-Huang, and K.-C. Chang, Reynolds number effect on compressible cylindrical cavity flow, Chin. J. Aeronaut. **33**, 456 (2020).
[57] See Supplemental Material at http://link.aps.org/supplemental/10.1103/dd1b-vlp7 for the four supplementary videos (1) Video of the high-repetition-rate PLRS and schlieren imaging highlighting the effect of $[L/D]$ at $[\Delta h/D] = 0$, $\mathrm{Re}_D = 74\,000$; (2) Video of the high-repetition-rate PLRS and schlieren imaging toward explaining the effect of Re_D for $[L/D] = 6$, $[\Delta h/D] = 0$; (3) Video of the high-repetition-rate PLRS and schlieren imaging portraying the effect of normalized excess rear face height $[\Delta h/D]$ at $\mathrm{Re}_D = 74\,000$ for $[L/D] = 6$; (4) Video presenting the differences in flow evolution between 2D and axisymmetric cavities through PLRS imaging for $[L/D] = 6$ at $\mathrm{Re}_D = 74\,000$.